Mechanical dissimilarity of defects in welded joints via Grassmann manifold and machine learning

David Ryckelynck, Thibault Goessel, Franck Nguyen

David Ryckelynck, Thibault Goessel, Franck Nguyen. Mechanical dissimilarity of defects in welded joints via Grassmann manifold and machine learning. 2020. ⟨hal-02559710v3⟩

HAL Id: hal-02559710
https://hal.science/hal-02559710v3

Preprint submitted on 23 Jul 2020

Mechanical dissimilarity of defects in welded joints via Grassmann manifold and machine learning

David Ryckelynck^a, **Thibault Goessel**^{b}, **Franck Nguyen**^{a}

a. Mines ParisTech PSL University, Centre des Matériaux, Evry | david.ryckelynck@mines-paristech.fr
b. Mines ParisTech PSL University | thibault.goessel@mines-paristech.fr

Keywords : Data encoding, Hyper-reduction, Reduced Order Model, ROM-net

Abstract

Assessing the harmfulness of defects based on images is becoming more and more common in industry. Today these defects can be inserted in digital twins that aim to replicate in a mechanical model what is observed on a component, so that an image-based diagnosis can be further conducted. But the variety of defects, the complexity of their shape and the computational complexity of finite element models related to their digital twin, make this kind of diagnosis too slow for any practical application. We show that a classification of observed defects enables the definition of a dictionary of digital twins. These digital twins prove to be representative for model reduction purposes, while preserving an acceptable accuracy for stress predictions. Non-supervised machine learning is used for both the classification issue and the construction of reduced digital twins. The dictionary items are medoids found by a k-medoids clustering algorithm. Medoids are supposed to be well distributed in the training dataset, according to a metrics or a dissimilarity measurement. In this paper, we propose a new dissimilarity measurement between defects. It is theoretically founded according to approximation errors in hyper-reduced predictions. In doing so, defect classes are defined according to their mechanical effect and not directly according to their morphology. In practice, each defect in the training dataset is encoded as a point on a Grassmann manifold. This methodology is evaluated through a test set of observed defects totally different from the training dataset of defects used to compute the dictionary of digital twins. The most appropriate item in the dictionary, for model reduction, is selected according to an error indicator related to the hyper-reduced prediction of stresses. No plasticity effect is considered here (merely isotropic elastic materials), which is a strong assumption but which is not critical for the purpose of the work. In spite of the large variety of defects, we show accurate predictions of stresses for most of defects in the test set.

Version française abrégée

L'évaluation de la nocivité des défauts à partir d'images est de plus en plus courante dans l'industrie. Aujourd'hui, ces défauts peuvent être insérés dans des jumeaux numériques qui visent à reproduire dans un modèle mécanique ce qui est observé sur un composant. Ainsi, un diagnostic à partir d'image peut être mis en place. Mais la variété des défauts, la complexité de leur forme et la complexité de calcul des modèles d'éléments finis liés à leur jumeau numérique, rendent ce type de diagnostic trop lent pour toute application pratique. Nous montrons dans cet article qu'une classification des défauts observés permet de définir un dictionnaire des jumeaux numériques. Ces jumeaux numériques se révèlent représentatifs pour la réduction de modèle, tout en conservant une précision acceptable pour la prévision des contraintes. Un apprentissage automatique non supervisé est utilisé à la fois pour la question de la classification et pour la construction de jumeaux numériques réduits. Les éléments du dictionnaire sont des médoïdes trouvés par l'algorithme de partitionnement k-médoïdes. Les médoïdes sont censés être bien répartis dans l'ensemble des données d'entraînement, selon une métrique ou une mesure de dissimilitude. Dans cet article, nous proposons une nouvelle mesure de dissimilitude entre les défauts. Elle est fondée théoriquement sur les erreurs d'approximation des prévisions hyperréduites. Ce faisant, les classes de défauts sont définies en fonction de leur effet mécanique et non directement en fonction de leur morphologie. En pratique, chaque défaut de l'ensemble de données d'entraînement est encodé comme un point sur une variété de Grassmann. Cette méthodologie est évaluée au moyen d'un ensemble de défauts tests totalement différents de l'ensemble de données d'apprentissage utilisé pour calculer le dictionnaire des jumeaux numériques. L'élément le plus approprié du dictionnaire, pour la réduction du modèle, est sélectionné en fonction d'un indicateur d'erreur lié à la prévision hyperréduite des contraintes. Aucun effet de plasticité n'est considéré ici (simplement des matériaux élastiques isotropes), ce qui est une hypothèse forte mais qui n'est pas critique pour l'objectif de ce travail. Malgré la grande variété de défauts, nous montrons des prévisions précises des contraintes pour la plupart des défauts de l'ensemble de test.

1 Introduction

Mechanical modeling based on images is becoming increasingly important in material science and in industrial applications for the assessment of defects harmfulness. The early detection of defects in industrial processes has been studied for more than a decade now. As a matter of fact, in 2011, scientists tried to improve the efficiency of early fault detection on gears, which are critical in many machinery operations [1]. Moreover, non-destructive inspection techniques are able to detect and locate voids for a wide range of materials and welding processes: resistance seam welding of aluminium, zinc and galvanised steel [2], resistance spot welding of ferritic/martensitic steels [3], electron beam welding of steel to Fe-Al alloy [4] or laser welding of stainless steels [5] and aluminium alloys [6].

Here, machine learning enhances the value of data related to defects observed in the past, if these data are available in a memory storage system. In the framework of image-based diagnosis, machine learning aims to consider the following assertions: if two defects are similar, they have equivalent harmfulness. Accounting for this similarity should facilitate the prediction of the harmfulness of new defects, by using a training dataset of defects. The purpose of this paper is to sample a training dataset of defects so that a set of representative defects is defined. The representative defects are supposed to be well distributed in the training dataset according to an appropriate metrics. This metrics classifies defects according to the displacement fluctuations they cause around them. Here, the sets of both experimental data and simulation data, related to the representative defects, define a dictionary of digital twins. This dictionary contains the simulation data for the construction of local reduced order bases [7] in the nonparametric space of observed defect. Next section presents a schematic view of these ideas.

Pure data-driven approaches have been detailed in literature for defect diagnosis. Provided that a wide range of data is available, machine learning methods can eventually detect automatically the defects and classify them in different classes, given a prescribed criteria. For instance, supervised machine learning is used for defect classification issues related to a freezing process in [8]. Convolutional Neural Networks (CNNs) [9], which are very helpful in computer vision [10], have been trained to detect and diagnose defects. In [11], a CNN detects defects on an automotive damper. Another encouraging study published recently uses CNNs to diagnose defects on freight trains, with a precision of around 80% [12]. An amazing property of CNNs is their ability to learn features, or kernels [10], solely by using labeled data and deep learning. But in our opinion, using deep learning does not necessarily imply to forget the available knowledge in mechanics of materials when it comes to predict defects harmfulness. The purpose of this paper is to couple machine learning and mechanical modeling so that a transfer learning [13] is achieved.

In mechanics of materials, image-based meshing methods [14, 15] enable to generate complex finite element meshes of digital images obtained via X-ray computed tomography [16]. The finite element models used as digital twins of mechanical components are fed by a huge knowledge on mechanical behavior for various materials, metals [17], composites [18] and concrete [19] for instance. Unfortunately, it cannot be used as a tool to assess the quality of a component in a serial production framework. The required fine meshes of defective components generally lead to prohibitive computational time as explained in [20]. But the use of mechanical knowledge in digital twins would ensure a data continuity between the component design phase and the diagnosis of defect harmfulness [20]. Besides, projection-based model order reduction methods enable to reuse knowledge in materials science while using machine learning to generate approximation spaces for a fast solution of partial differential equations [21, 22]. Therefore, physics principles and material constitutive equations are preserved in weak formulations of partial derivative equations. In this paper, the machine learning task is restricted to the construction of an approximation space, for model order reduction purpose. Here this approximation space is piece-wise constant over the space of all possible defects. Its numerical representation is a dictionary of digital twins based on representative defects. Usually, the manifold containing the solution of a partial differential equation (PDE) can be accurately depicted as living in a small vector space. Therefore, linear machine learning methods, like the proper orthogonal decomposition [23] or the singular value decomposition or non centered principal component analysis, aim at learning this reduced vector space from simulation data. This sub-space is then used as a single approximation space for projection-based model order reduction of PDE. In practice, the finite element shape functions are replaced by vectors, or empirical modes, that span the reduced approximation space. In some situations, the solution of the governing PDEs lies in a manifold which cannot be covered by a single vector sub-space without increasing its dimension and thus degrading the computational complexity of projection-based model reduction. In these cases, deep learning algorithms are useful to reduce the complexity of approximation spaces by using simulation data. For instance, in [24], physics-informed neural networks are proposed to solve supervised learning tasks while respecting any given laws of physics described by general nonlinear partial differential equations. These networks are no more projection-based model order reduction schemes. But such reduced schemes are found in [25] and [22], where a deep classifier recommends a reduced order model depending on input variables having a tensor format (i.e. images for instance). In [25], a CNN recommends a reduced order model related to a loading environment seen on an image of an experimental setup. In [22], a deep classifier using CNN is trained to recommend hyper-reduced order models for lifetime prediction depending on a 3D stochastic temperature field. These two contributions follow the same neural network architecture, termed ROM-net [22]. Such ROM-net are trained by using simulation data encoded as points on a Grassmann manifold, which is a set of vector sub-spaces of given common dimensions in the same ambient space. This data encoding is quite general when considering simulation data in the framework of projection-based model order reduction. In this paper, it is extended for the classification of voids according to their mechanical effects in mechanical components.

In the current work, observational data are 2D slices of experimental 3D images of voids. These 3D images have been obtained via X-ray computed tomography by L. Lacourt [26]. The reduced approximation space for displacements is span by two sorts of vectors: macroscopic modes of an ideal defect-free medium, and fluctuation modes around each defect. By following the two-scale machine learning approach proposed in [20], the fluctuation modes are computed by assuming dilution conditions and scale separation for each defect, separately. The volume fraction of the defect is negligible when computing the fluctuation modes. In linear elasticity, each defect admits an exact reduced basis of fluctuation modes for strains and displacements. For 2D problems, this ideal reduced basis contains 3 modes, in 3D it contains 6 modes. This reduced basis is named ideal because its computation requires the finite element solution of an elastic problem which is specific to the defect. In the proposed approach, such solutions are available only during the training phase of the approximation space. In the test phase, the ideal reduced basis is not available. The methodology, introduced in [22] for ROM-nets, aims to take in a dictionary the reduced approximation space related to a similar defect as a substitute to the ideal reduced basis. Here, this dictionary is named dictionary of digital twins. This requires to define:

- a dissimilarity evaluation between defects,
- a dictionary of representative defects containing the related digital twins, with a small number of items,
- a classifier that finds the best item in the dictionary for the construction of an approximation space dedicated to the target digital twin in a test set or for real application.

In this paper, the representative defects are medoids selected by the k-medoids algorithm [27]. The number of medoids has to be prescribed prior the data clustering via the k-medoids algorithm. Too many items in the dictionary make the classifier too complex, and would eventually entail no complexity reduction for image-based modeling. In this paper, the best item in the dictionary is approximately selected via an error indicator and not via a CNN as proposed in [22]. This error indicator measures the discrepancy between the stresses predicted via hyper-reduction for the target digital twin and the equilibrated stresses. A theoretical analysis of the convergence of the hyper-reduced approximation shows that a partial approximation error has an upper bound that scales linearly with the sinus of the principal angles between the ideal modes and the modes involved in the approximation space. Identical reduced bases have principal angles equal to zero, as well as sinus. The convenient space to measure these angles is a Grassmann manifold [28, 29]. The sinus of these angles is termed Chordal distance [30]. Hence, the proposed dissimilarity criterion accounts for the mechanical effect of the defects, via model reduction of displacement fluctuations around defects. It is not a direct evaluation of the morphology dissimilarity.

For the sake of simplicity, the target problem used for defect diagnosis is similar to the micromechanical problem that defines the fluctuation modes. The reader can find in [20] more complex target mechanical problems that are solved by the hyper-reduction method used in this paper. The finite element approximation space being specific to each defect, we need to design a common ambient space for the computation of Grassmann distances. It is performed through an encoding mesh. We have paid a particular attention to the compromise to be made between the accuracy of the numerical approximations and the memory space required to save the simulation data related to the encoding mesh.

The present paper is structured as follows. Section 2 is a commented graphical abstract. Section 3 presents the projection-based model reduction method, an upper bound for partial errors on displacement predictions and the encoding mesh associated to the Grassmann manifold. Section 4 presents the training dataset of defects, the partition of these data by using the k-medoids algorithm in the Grassmann manifold and some validation results. Section 5 shows the stress predictions results for the test set of defects and the classifier used to select an item in the dictionary of digital twins. Section 6 is the conclusion of this paper.

2 Commented graphical abstract

Suppose a training dataset of defects is available with detailed digital twins and all related data. A schematic view of the training dataset is plotted in Figure 1. Training data are plotted as blue points in this figure.

We propose to select representative defects and their data in order to form a dictionary of digital twins for model reduction purpose. Representative defects are supposed to be well distributed in the training dataset, according to a dissimilarity measurement. Two representative defects are spotted in red and green in Figure 1. The main novelty is a proper dissimilarity definition between defects, so that the representative defects are medoids selected by using the k-medoids algorithm [27].

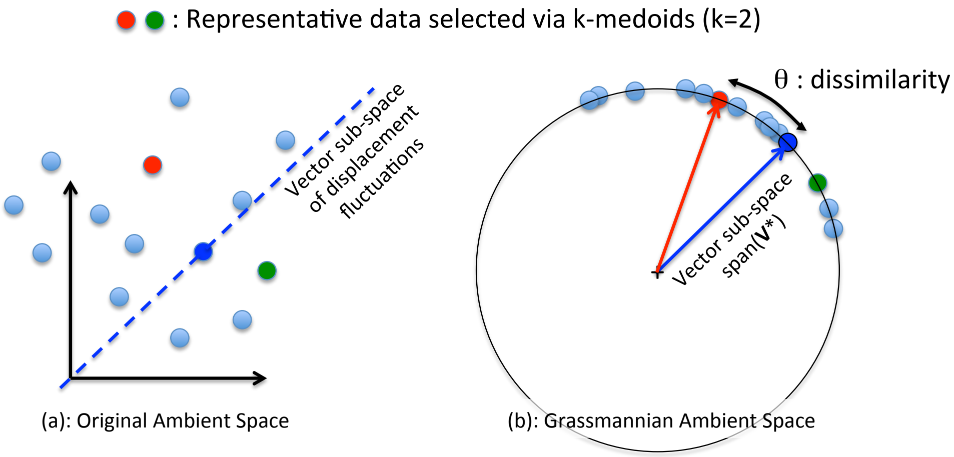

(a): Original Ambient Space

(b): Grassmannian Ambient Space

Figure 1: (a) Raw data in their original ambient space, (b) the proposed ambient space for dissimilarity measurement between defects according to a Grassmann distance related to the sub-space spanned by fluctuation modes around each defect.

The original ambient space, (a) in Figure 1, that contains the predictions of fluctuations around defects in the training dataset, does not account for the linearity of elastic balance equations. We know that displacement fluctuations belong to a small vector sub-space spanned by fluctuation modes, denoted by $\mathbf{V}^\star$ for each defect individually. These vector sub-spaces are points in a manifold termed Grassmannian. As a resut, prior dissimilarity computation between defects, the training data are placed in a proper ambient space: a Grassmannian. A sketch of the Grassmannian ambient space is shown in part (b) of Figure 1.

Displacement fluctuations or stress fluctuations around defects, have magnitudes directly related to the loading magnitude defined in the mechanical target problem. They can be easily computed. That is the reason why fluctuation magnitudes do not matter in similar linear predictions. Then the Grassmannian ambient space is plotted as a unit circle. The geodesic distance on this circle is the angle θ shown in Figure 1 (b). One can also consider, in Figure 1, the Chordal distance which is the length of the straight line between two points on this circle for small values of θ. This Chordal distance is closely related to an upper bound of partial approximation errors.

In the sequel, the simulation data of the representative defects are the training data used for the hyper-reduction of digital twins.

Data in the test set cannot be plotted in Figure 1, because their related fluctuation fields have to be predicted via the proposed dictionary-based model-reduction method.

3 Theoretical results on elastic fluctuation modes

3.1 Projection-based hyper-reduction of the target mechanical problem

This section describes the target mechanical problem used as a digital twin of a target defect. In mechanics of materials, the harmfulness of defect is evaluated through the magnification of Cauchy stress around each defect. We restrict our attention to the prediction of the Cauchy stress via the approximate solution of partial differential equations in linear elasticity of isotropic materials. The principal variable of these equations is the displacement field.

The domain occupied by the material, denoted by $\Omega^\star$, is a surrounding box around each defect. We give an example in Figure 2. Formally, $\Omega^\star$ has no parameter. Its morphology totally depends on the observation of a defect through a digital image. In the following, the superscript $\star$ refers to mathematical objects that are specific to a digital image of a defect. This notation emphasizes the variability due to the input image. All mathematical objects with the superscript $\star$ can be seen as the output of an implicit function depending on $\Omega^\star$, without introducing any parameter for $\Omega^\star$. We avoid giving a morphological definition of an input space that contains all possible $\Omega^\star$. Hence, the proposed setting is a non-parametric mechanical modeling for digital twins.

The outer boundary of the surrounding box is denoted by $\partial_E \Omega^\star$. The boundary of the defect, which is modeled as a void, is denoted by $\partial_V \Omega^\star$. The local frame follows the principal axes of the second-order moments of the volume distribution in the defect. These principal axes are denoted by $\mathbf{e}_1$ and $\mathbf{e}_2$. All defects have a circumscribed circle of diameter equal to D. The length of $\Omega^\star$ is $30\,D$. The displacement field and the Cauchy stress are denoted by $\mathbf{u}^\star$ and $\boldsymbol{\sigma}^\star$ respectively. The fluctuation of the displacement field is denoted by $\Delta\mathbf{u}^\star$. It is defined as the counterpart of the homogeneous displacement field such that:

$$\mathbf{u}^\star(\mathbf{x}) = \mathbf{E} \,.\, \mathbf{x} + \Delta\mathbf{u}^\star(\mathbf{x}) \quad \forall \mathbf{x} \in \Omega^\star, \quad \Delta\mathbf{u}^\star \in \mathcal{V}^\star \tag{1}$$

where $\mathbf{E}$ is a macroscopic strain tensor imposed on $\partial_E \Omega^\star$. It is a given symmetric second order tensor. $\mathbf{E} \,.\, \mathbf{x}$ is a defect-free macroscopic mode for displacements. $\mathcal{V}^\star$ is an usual finite element approximation space that accounts for the defect geometry and Dirichlet boundary conditions (2) on $\partial_E \Omega^\star$.

$\Omega^\star$ is large enough to fulfill a dilution assumption and the following boundary condition on $\Delta\mathbf{u}^\star$:

$$\Delta\mathbf{u}^\star(\mathbf{x}) = 0, \quad \forall \mathbf{x} \in \partial_E \Omega^\star \tag{2}$$

The Hooke tensor for elasticity is denoted by $\mathbf{C}$. Hence, the elastic constitutive equation reads:

$$\boldsymbol{\sigma}^\star = \mathbf{C} \;:\; \boldsymbol{\varepsilon}(\mathbf{u}^\star) \tag{3}$$

where $\boldsymbol{\varepsilon}(\mathbf{u}^\star)$ is the deformation tensor, i.e. the symmetric part of the displacement gradient. The weak form of the elastic equilibrium equation reads: find $\Delta\mathbf{u}^\star \in \mathcal{V}^\star$ such that,

$$\Delta\mathbf{u}^\star(\mathbf{x}) = \sum_{i=1}^{\mathcal{N}^\star} \boldsymbol{\varphi}_i^\star(\mathbf{x})\, q_i^\star, \; \forall \mathbf{x} \in \Omega^\star \tag{4}$$

$$\int_{\Omega^\star} \boldsymbol{\varepsilon}(\boldsymbol{\varphi}_i^\star) \;:\; \mathbf{C} \;:\; (\mathbf{E} + \boldsymbol{\varepsilon}(\Delta\mathbf{u}^\star)) \; d\Omega = 0 \quad \forall i \in \{1, \ldots, \mathcal{N}^\star\} \tag{5}$$

where $(\boldsymbol{\varphi}_i^\star)_{i=1}^{\mathcal{N}^\star}$ are the finite element shape functions that span $\mathcal{V}^\star$, such that $\boldsymbol{\varphi}_i^\star = 0$ on $\partial_E \Omega^\star$. $\mathbf{E}$ being a symmetric second order tensor, it has only three components for 2D problems. Therefore, the elastic equations being linear, it exists an ideal reduced basis containing three fluctuation modes denoted by $(\boldsymbol{\psi}_k^\star)_{k=1,\ldots,3}$ such that:

$$\Delta\mathbf{u}^\star(\mathbf{x}) = \sum_{k=1}^{N} \boldsymbol{\psi}_k^\star(\mathbf{x})\, \overline{\gamma}_k^\star, \; \forall \mathbf{x} \in \Omega^\star, \quad \boldsymbol{\psi}_k^\star \in \mathcal{V}^\star, \; k = 1, \ldots, N \tag{6}$$

where $\overline{\gamma}^\star \in \mathbb{R}^3$ is a vector of exact reduced coordinates. The fluctuations modes being vectors of the approximation space, one can introduce the reduction matrix $\mathbf{V}^\star$, that contains the finite element coordinates of the fluctuation modes:

$$\boldsymbol{\psi}_k^\star(\mathbf{x}) = \sum_{i=1}^{\mathcal{N}^\star} \boldsymbol{\varphi}_i^\star(\mathbf{x})\, V_{ik}^\star, \quad k = 1, 2, 3, \; \forall \mathbf{x} \in \Omega^\star \tag{7}$$

In the sequel, approximate reduced bases for fluctuation modes are denoted by $\mathbf{V}$. In Figure 1 (b), $\mathbf{V}^\star$ is the blue arrow and $\mathbf{V}$ is the red arrow. $\mathbf{V}$ may be not totally specific to $\Omega^\star$. The approximate continuous modes are:

$$\boldsymbol{\psi}_k(\mathbf{x}) = \sum_{i=1}^{\mathcal{N}^\star} \boldsymbol{\varphi}_i^\star(\mathbf{x})\, V_{ik}, \quad k = 1, 2, 3, \; \forall \mathbf{x} \in \Omega^\star \tag{8}$$

For a given reduced matrix $\mathbf{V}$, the approximate displacement fluctuation reads:

$$\Delta\mathbf{u}(\mathbf{x}) = \sum_{k=1}^{N} \boldsymbol{\psi}_k(\mathbf{x})\, \gamma_k, \; \forall \mathbf{x} \in \Omega^\star \tag{9}$$

The two reduced bases span two vector spaces of same dimension N in the same ambient space $\mathbb{R}^{\mathcal{N}^\star}$, $N < \mathcal{N}^\star$. Each of these vector spaces is a point in a Grassmann manifold, denoted by $Gr(N, \mathcal{N}^\star)$. This manifold is a huge space, as it contains all the vector sub-spaces of dimension N in $\mathbb{R}^{\mathcal{N}^\star}$. For instance, it contains also the vector sub-spaces spanned by all sets of N vibration modes. Such vibration modes are not relevant here. But, the Grassmann manifold is equipped with a geodesic metrics, which is very convenient for the definition of the dissimilarity between defects as explained in the next section, when considering approximation errors due to the hyper-reduction method.

The hyper-reduction (HR) method [31] aims at computing reduced coordinates $\boldsymbol{\gamma}$ introduced in Equation (9), by projecting the equilibrium equation on $\mathbf{V}$, via a restriction of the domain $\Omega^\star$ to a reduced integration domain (RID) denoted by $\Omega^\star_R$. By following the empirical interpolation method [32], interpolation points are computed for column vectors in $\mathbf{V}$. We choose the RID $\Omega^\star_R$ such that it contains the interpolation points related to both the reduced basis for displacement and a reduced basis for stresses. We give more details about the construction of $\Omega^\star_R$ in Appendix. We define, a set of test reduced functions denoted by $\boldsymbol{\psi}_{R\,j}$:

$$
\begin{aligned}
\mathcal{F} &= \left\{ i \in \{1, \dots, \mathcal{N}^\star\},\ \int_{\Omega^\star \backslash \Omega_{R^\star}} (\boldsymbol{\varphi}^\star_i)^2 \, d\Omega = 0 \right\} && (10) \\
\boldsymbol{\psi}_{R\,j}(\mathbf{x}) &= \sum_{i \in \mathcal{F}}^{\mathcal{N}^\star} \boldsymbol{\varphi}^\star_i(\mathbf{x}) \, V_{ij}, \quad \forall \mathbf{x} \in \Omega^\star,\ j = 1, 2, 3 && (11)
\end{aligned}
$$

As explained in [31], these test functions are null on the interface between $\Omega^\star_R$ and the counterpart of the domain, as if Dirichlet boundary conditions were imposed. On this interface, the displacement follows the shape of the modes $\boldsymbol{\psi}_k$. The hyper-reduction method gives access to reduced coordinates $\boldsymbol{\gamma}$ that fulfill the following balance equations:

$$
\Delta \mathbf{u}(\mathbf{x}) = \sum_{k=1}^{N} \boldsymbol{\psi}_k(\mathbf{x}) \, \gamma_k, \ \forall \mathbf{x} \in \Omega^\star_R \tag{12}
$$

$$
\int_{\Omega^\star_R} \boldsymbol{\varepsilon}(\boldsymbol{\psi}_{R\,j}) \ : \ \mathbf{C} \ : \ (\mathbf{E} + \boldsymbol{\varepsilon}(\Delta \mathbf{u})) \ d\Omega = 0, \quad \forall j = 1, \dots, N \tag{13}
$$

The matrix form of the hyper-reduced balance equations reads: find $\boldsymbol{\gamma} \in \mathbb{R}^N$ such that,

$$
\begin{aligned}
\Delta \mathbf{u}(\mathbf{x}) &= \sum_{i=1}^{\mathcal{N}^\star} \boldsymbol{\varphi}^\star_i(\mathbf{x}) \, q^{HR}_i, \ \forall \mathbf{x} \in \Omega^\star_R && (14) \\
\mathbf{q}^{HR} &= \mathbf{V} \, \boldsymbol{\gamma} && (15) \\
\mathbf{K}^{HR} \, \boldsymbol{\gamma} &= \mathbf{V}[\mathcal{F}, :]^T \, \mathbf{F}^\star[\mathcal{F}] && (16) \\
\mathbf{K}^{HR} &= \mathbf{V}[\mathcal{F}, :]^T \, \mathbf{K}^\star[\mathcal{F}, :] \, \mathbf{V} && (17) \\
K^\star_{ij} &= \int_{\Omega^\star} \boldsymbol{\varepsilon}(\boldsymbol{\varphi}^\star_i) \ : \ \mathbf{C} \ : \ \boldsymbol{\varepsilon}(\boldsymbol{\varphi}^\star_j) \, d\Omega, \ i, j = 1, \dots, \mathcal{N}^\star && (18) \\
F^\star_i &= -\int_{\Omega^\star} \boldsymbol{\varepsilon}(\boldsymbol{\varphi}^\star_i) \ : \ \mathbf{C} \ : \ \mathbf{E} \, d\Omega, \ i = 1, \dots, \mathcal{N}^\star && (19)
\end{aligned}
$$

where $\mathbf{V}[\mathcal{F}, :]$ denotes a row restriction of matrix $\mathbf{V}$ to indices in $\mathcal{F}$. We assume that the matrix $\mathbf{K}^{HR}$ is full rank. This assumption is always checked in numerical solutions of hyper-reduced equations. Rank deficiency may appear when the RID construction do not account for the contribution of a reduced basis dedicated to stresses.

In this paper, the hyper-reduced prediction is supplemented by the following equilibrium step over the RID: find $\delta \mathbf{u}^\star$ such that,

$$
\delta \mathbf{u}^\star(\mathbf{x}) = \sum_{i \in \widetilde{\mathcal{F}}} \boldsymbol{\varphi}^\star_i(\mathbf{x}) \, \delta q^\star_i, \ \forall \mathbf{x} \in \Omega^\star_R \tag{20}
$$

$$
\int_{\Omega^\star_R} \boldsymbol{\varepsilon}(\boldsymbol{\varphi}^\star_i) \ : \ \mathbf{C} \ : \ (\mathbf{E} + \boldsymbol{\varepsilon}(\Delta \mathbf{u} + \delta \mathbf{u}^\star)) \ d\Omega = 0 \quad \forall i \in \widetilde{\mathcal{F}} \tag{21}
$$

where $\widetilde{\mathcal{F}}$ is the set of all degrees of freedom in $\Omega_R^\star$ excepted those belonging to elements connected to the interface between $\Omega_R^\star$ and its counterpart. During this correction step, displacements are frozen on elements connected to the interface between $\Omega_R^\star$ and its counterpart. There is no natural boundary condition on this interface. They are here forecast by the hyper-reduced prediction. This correction step has been proposed in [33] for the evaluation of contact forces. This is a local correction step over $\Omega_R^\star$. The solution $\mathbf{u}^{eq} = \mathbf{E}\,\mathbf{x} + \Delta\mathbf{u} + \delta\mathbf{u}^\star$ is an hybrid solution that weakly couples hyper-reduction and a finite element approximation over the RID. We refer the reader to [33, 34, 35] for more details about hybrid hyper-reduction schemes. The equilibrated stress is quite accurate compared to the stress computed via hyper-reduction solely. The hyper-reduced stress prediction is denoted by $\boldsymbol{\sigma}^{HR}$, while the equilibrated stress is denoted by $\boldsymbol{\sigma}^{eq}$. $\delta\boldsymbol{\sigma}^\star$ is the correction term for stress predictions:

$$\begin{aligned}
\boldsymbol{\sigma}^{HR} &= \mathbf{C} \,:\, (\mathbf{E} + \varepsilon(\Delta\mathbf{u})) && (22)\\
\delta\boldsymbol{\sigma}^\star &= \mathbf{C} \,:\, \varepsilon(\delta\mathbf{u}^\star) && (23)\\
\boldsymbol{\sigma}^{eq} &= \boldsymbol{\sigma}^{HR} + \delta\boldsymbol{\sigma}^\star && (24)
\end{aligned}$$

Property 1: If $\mathbf{K}^{HR}$ is full rank, then the hyper-reduced balance equations are equivalent to an oblique projection of the finite element prediction:

$$\mathbf{q}^{HR} = \mathbf{V}\,(\boldsymbol{\Pi}^T\,\mathbf{V})^{-1}\boldsymbol{\Pi}^T\,\mathbf{q}^\star \tag{25}$$

with $\boldsymbol{\Pi} = \mathbf{K}^\star[:,\mathcal{F}]\,\mathbf{V}[\mathcal{F},:]$. Hence the hyper-reduced prediction of the reduced coordinates vector $\boldsymbol{\gamma}$ is a minimizer for $f(\boldsymbol{\beta})$:

$$\boldsymbol{\beta} \in \mathbb{R}^N,\ f(\boldsymbol{\beta}) = \|\boldsymbol{\Pi}^T\ (\mathbf{V}\,\boldsymbol{\beta} - \mathbf{q}^\star)\,\|_2^2 \tag{26}$$

Here $\boldsymbol{\Pi}$ is a projector for elastic stresses in $\Omega_R^\star$ according to the reduced test functions:

$$\sum_{i=1}^{\mathcal{N}^\star} \Pi_{ik}\ (\mathbf{V}\,\boldsymbol{\gamma} - \mathbf{q}^\star)_i = \int_{\Omega_R^\star} \varepsilon(\boldsymbol{\psi}_{R\,k})\ :\ \left(\boldsymbol{\sigma}^{HR} - \boldsymbol{\sigma}^\star\right)\, d\Omega \tag{27}$$

where $\boldsymbol{\sigma}^\star$ is the finite-element stress prediction.

The proof is straightforward. Here, $\mathbf{K}^{HR} = \boldsymbol{\Pi}^T\mathbf{V}$. The Jacobian matrix for f reads $\mathbf{J} = \mathbf{V}^T\boldsymbol{\Pi}\boldsymbol{\Pi}^T\mathbf{V} = (\mathbf{K}^{HR})^T\,\mathbf{K}^{HR}$. If $\mathbf{K}^{HR}$ is full rank, then $\mathbf{J}$ is symmetric definite positive and $\mathbf{J}^{-1} = (\mathbf{K}^{HR})^{-1}\,(\mathbf{K}^{HR})^{-T}$. Then, both the minimization problem and the hyper-reduced equation have a unique solution. The solution of the minimization problem is:

$$\begin{aligned}
\mathbf{q}^f &= \mathbf{V}\,(\mathbf{J})^{-1}\mathbf{V}^T\,\boldsymbol{\Pi}\,\boldsymbol{\Pi}^T\,\mathbf{q}^\star && (28)\\
&= \mathbf{V}\,(\mathbf{K}^{HR})^{-1}\,\boldsymbol{\Pi}^T\,\mathbf{q}^\star && (29)
\end{aligned}$$

Since $\boldsymbol{\Pi}^T\,\mathbf{q}^\star = \mathbf{V}[\mathcal{F},:]^T\,\mathbf{F}^\star[\mathcal{F}]$, $\mathbf{q}^f = \mathbf{q}^{HR}$.

We can notice that, if $\Omega_R^\star = \Omega^\star$, $\widetilde{\mathcal{F}}$ contains all degrees of freedom indices and $\delta\mathbf{u}^\star = \Delta\mathbf{u}^\star - \Delta\mathbf{u}$. But the correction step has the same computational complexity as the full finite element model. In our case, the size of $\Omega^\star$ has been carefully chosen so that the reduction in complexity is not trivial. Here the most complex operations are indeed the computation of $\mathbf{K}^{HR}$ and the solution of the reduced linear system of equations. They respectively scale linearly with $\mathrm{card}(\mathcal{F})\ N^2$ and N^3. Hence N^3 has to be small enough compared to $\mathcal{N}^\star$ if we consider the computational complexity for the solution of sparse linear systems in the finite element method.

3.2 Approximation errors

Let's introduce the three canonical macroscopic strains, $\mathbf{E}^{(1)}$, $\mathbf{E}^{(2)}$, $\mathbf{E}^{(3)}$:

$$\begin{aligned}
\mathbf{E}^{(1)} &= \varepsilon(x_1\,\mathbf{e}_1) && (30)\\
\mathbf{E}^{(2)} &= \varepsilon(x_2\,\mathbf{e}_2) && (31)\\
\mathbf{E}^{(3)} &= \varepsilon(\frac{x_1\,\mathbf{e}_2 + x_2\,\mathbf{e}_1}{2}) && (32)
\end{aligned}$$

In the sequel, the three finite element solutions obtained for each canonic macroscopic strains $\mathbf{E}^{(1)}$, $\mathbf{E}^{(2)}$, $\mathbf{E}^{(3)}$, are saved in a matrix $\mathbf{Q}^\star$ such that the three displacement fields read:

$$\mathbf{u}^{\star(j)}(\mathbf{x}) = \mathbf{E}^{(j)} \,.\, \mathbf{x} + \Delta\mathbf{u}^{\star(j)}(\mathbf{x}) \quad \forall \mathbf{x} \in \Omega^\star,\ j = 1,2,3 \tag{33}$$

$$\Delta\mathbf{u}^{\star(j)}(\mathbf{x}) = \sum_{i=1}^{\mathcal{N}^\star} \varphi_i^\star(\mathbf{x})\, Q_{ij}^\star, \quad \forall \mathbf{x} \in \Omega^\star,\ j = 1,2,3 \tag{34}$$

All mechanical simulations are run with the Z-Set software suite. One can find more information on this website : http://www.zset-software.com/. The reduced basis $\mathbf{V}^\star$ is obtained by using a truncated singular value decomposition (SVD) of $\mathbf{Q}^\star$:

$$\mathbf{Q}^\star = \mathbf{V}^\star\, \mathbf{S}^\star\, \mathbf{W}^{\star T}, \quad \mathbf{V}^\star \in \mathbb{R}^{\mathcal{N}^\star \times 3},\ \mathbf{V}^{\star\,T}\, \mathbf{V}^\star = \mathbf{I} \tag{35}$$

where $\mathbf{I}$ is the 3×3 identity matrix. Because of linearity of the elastic problem above, $\mathbf{C}$ is proportional to the Young modulus, hence $\mathbf{V}^\star$ does not depend on the value of the Young modulus, thanks to the normalization of the modes. Regarding the Poisson coefficient, for the sake of simplicity, we restrict our attention to isotropic materials having a Poisson coefficient equal to 0.3. An example of displacement fluctuations is shown in Figure 2.

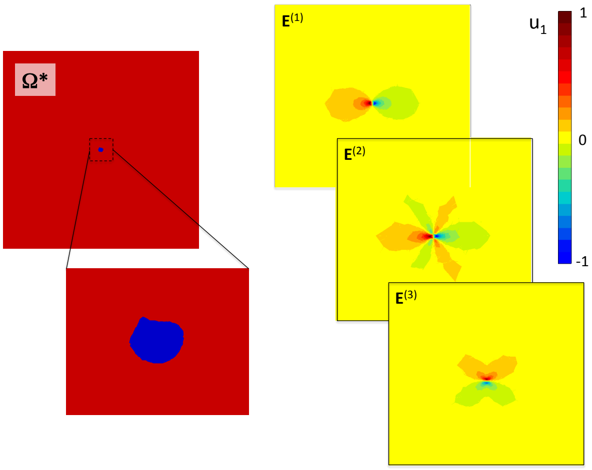

Figure 2: On the left, an experimental defect and a zoom on it. On the right, the horizontal component of $\Delta u^{\star(j)}$, for 2 traction modes related to $\mathbf{E}^{(1)}$ and $\mathbf{E}^{(2)}$, and one shearing mode related to $\mathbf{E}^{(3)}$

Similarly to Céa's lemma, but in finite dimension, it exists an upper bound for the approximation error observed through the projector $\mathbf{\Pi}$. The best projection of the exact solution in the approximation space via the 2-norm is denoted by γ_P:

$$\gamma_P = \text{argmin}_{\mathbf{q}=\mathbf{V}\,\mathbf{g}} \|\mathbf{q}^\star - \mathbf{q}\|_2^2 \tag{36}$$

with $\mathbf{q}^\star = \mathbf{V}^\star\, \overline{\gamma}^\star$ and $\mathbf{K}^\star\, \mathbf{q}^\star = \mathbf{F}^\star$. Hence $\gamma_P = \mathbf{V}^T\, \mathbf{V}^\star\, \overline{\gamma}^\star$.

Property 2: It exists a stability coefficient $c^\star$, that does not depend on $\mathbf{F}^\star$ (the loading condition), such that the partial approximation error has the following upper bound:

$$\|\mathbf{\Pi}^T\, (\mathbf{q}^\star - \mathbf{V}\,\gamma)\|_2 \leq c^\star\, \|\mathbf{q}^\star - \mathbf{V}\,\gamma_P\|_2 \tag{37}$$

where $\|\mathbf{\Pi}^T\, (\mathbf{q}^\star - \mathbf{V}\,\gamma)\|_2$ is a partial approximation error that does not account for errors in stress predictions outside $\Omega_R^\star$. Hence, the smaller the Euclidian distance between the sub-space span by $\mathbf{V}$ and the finite element prediction, the better the prediction of the stress in $\Omega_R^\star$ according to the projector $\mathbf{\Pi}$. it is therefore relevant to train $\mathbf{V}$ by using a training dataset of defects. When the RID covers the full domain, a certification of the reduced projection can be achieved, where all errors admit an upper bound, by following the constitutive relation error proposed in [36, 37].

The proof of the previous property is straightforward in finite dimension. Let's denote by $\alpha^\star$ an upper bound of the highest singular value of $\mathbf{\Pi}$. Then:

$$\|\mathbf{\Pi}^T\,(\mathbf{q}^\star - \mathbf{q})\|_2^2 \leq (\alpha^\star)^2\,\|\mathbf{q}^\star - \mathbf{q}\|_2^2 \quad \forall\,\mathbf{q}$$

Moreover, $\boldsymbol{\gamma}$ being a minimizer for $f(\cdot)$, we obtain:

$$\|\mathbf{\Pi}^T\,(\mathbf{q}^\star - \mathbf{V}\,\gamma)\|_2^2 \leq \|\mathbf{\Pi}^T\,(\mathbf{q}^\star - \mathbf{V}\,\gamma_P)\|_2^2 \tag{38}$$

and:

$$\|\mathbf{\Pi}^T\,(\mathbf{q}^\star - \mathbf{V}\,\gamma)\|_2^2 \leq (\alpha^\star)^2\,\|\mathbf{q}^\star - \mathbf{V}\,\gamma_P\|_2^2 \tag{39}$$

Property 3: If $\mathbf{V}^\star \in \mathbb{R}^{\mathcal{N}^\star\times N}$ and $\mathbf{V} \in \mathbb{R}^{\mathcal{N}^\star\times N}$ are two orthonormal matrices of the same ambient space $\mathbb{R}^{\mathcal{N}^\star}$, then they span sub-spaces that belong to the same Grassmann manifold. The partial approximation error has an upper bound depending on the Chordal distance [30], denoted by $d^{Ch}(\mathbf{V}^\star, \mathbf{V})$, between the sub-spaces span by $\mathbf{V}^\star$ and $\mathbf{V}$ respectively:

$$\|\mathbf{\Pi}^T\,(\mathbf{q}^\star - \mathbf{V}\,\gamma)\|_2 \leq \alpha^\star\,d^{Ch}(\mathbf{V}^\star, \mathbf{V})\,\sqrt{N}\,\|\overline{\gamma}^\star\|_2 \tag{40}$$

where the Chordal distance [30] uses the principal angles $\boldsymbol{\theta} \in \mathbb{R}^N$, $\theta_k \in [0, \pi/2[$ for $k = 1, \dots N$, computed via the following singular value decomposition:

$$\begin{aligned}
\mathbf{V}^T\,\mathbf{V}^\star &= \mathbf{U}\,\cos(\boldsymbol{\theta})\mathbf{U}^{\star T}, \quad \mathbf{U}^T\mathbf{U} = \mathbf{U}^{\star T}\mathbf{U}^\star = \mathbf{I} && (41)\\
d^{Ch}(\mathbf{V}^\star, \mathbf{V}) &= \|\sin(\boldsymbol{\theta})\|_F && (42)\\
\|\mathbf{U}^\star\|_F^2 &= N && (43)
\end{aligned}$$

where $\|\cdot\|_F$ is the Frobenius norm. Here, $\cos(\boldsymbol{\theta})$ and $\sin(\boldsymbol{\theta})$ are cosine and sine diagonal matrices. In addition the following property holds when a full SVD is computed:

$$\mathbf{U}^\star\,\mathbf{U}^{\star T} = \mathbf{I} \tag{44}$$

The proof is the following:

$$\|\mathbf{q}^\star - \mathbf{V}\,\gamma_P\|_2^2 = \overline{\gamma}^{\star T}\,(\mathbf{V}^\star - \mathbf{V}\,\mathbf{V}^T\,\mathbf{V}^\star)^T\,(\mathbf{V}^\star - \mathbf{V}\,\mathbf{V}^T\,\mathbf{V}^\star)\,\overline{\gamma}^\star = \overline{\gamma}^{\star T}\,(\mathbf{I} - \mathbf{V}^{\star T}\mathbf{V}\,\mathbf{V}^T\,\mathbf{V}^\star)\,\overline{\gamma}^\star \tag{45}$$

Hence:

$$\|\mathbf{q}^\star - \mathbf{V}\,\gamma_P\|_2^2 = \overline{\gamma}^{\star T}\,(\mathbf{I} - \mathbf{U}^\star\,\cos(\boldsymbol{\theta})^2\,\mathbf{U}^{\star T})\,\overline{\gamma}^\star \tag{46}$$

$$\|\mathbf{q}^\star - \mathbf{V}\,\gamma_P\|_2^2 = \overline{\gamma}^{\star T}\,\mathbf{U}^\star(\mathbf{I} - \cos(\boldsymbol{\theta})^2)\,\mathbf{U}^{\star T}\,\overline{\gamma}^\star \tag{47}$$

$$\begin{aligned}
\|\mathbf{q}^\star - \mathbf{V}\,\gamma_P\|_2^2 &= \overline{\gamma}^{\star T}\,\mathbf{U}^\star\sin(\boldsymbol{\theta})^2\,\mathbf{U}^{\star T}\,\overline{\gamma}^\star && (48)\\
&= \|\sin(\boldsymbol{\theta})\,\mathbf{U}^{\star T}\,\overline{\gamma}^\star\|_2^2 && (49)\\
& && (50)
\end{aligned}$$

For all matrices $\mathbf{A} \in \mathbb{R}^{n\times m}$ and $\mathbf{B} \in \mathbb{R}^{m\times n}$ the following property holds:

$$\|\mathbf{AB}\|_F \leq \|\mathbf{A}\|_F\,\|\mathbf{B}\|_F$$

and for $\mathbf{a} \in \mathbb{R}^n$: $\|\mathbf{a}\|_F = \|\mathbf{a}\|_2$
Thus:

$$\|\mathbf{q}^\star - \mathbf{V}\,\gamma_P\|_2^2 \leq \|\sin(\boldsymbol{\theta})\,\mathbf{U}^{\star T}\|_F^2\,\|\overline{\gamma}^\star\|_2^2 \leq \|\sin(\boldsymbol{\theta})\|_F^2\,N\,\|\overline{\gamma}^\star\|_2^2 \tag{51}$$

and

$$\|\mathbf{\Pi}^T\,(\mathbf{q}^\star - \mathbf{V}\,\gamma)\|_2 \leq \alpha^\star\,\|\sin(\boldsymbol{\theta})\|_F\,\sqrt{N}\,\|\overline{\gamma}^\star\|_2 \tag{52}$$

Property 3 is a convergence property for hyper-reduced predictions. If $\boldsymbol{\theta} = 0$, then $\mathbf{V}\,\mathbf{U} = \mathbf{V}^\star\,\mathbf{U}^\star$ and:

$$\begin{aligned} 0 &= \boldsymbol{\Pi}^T\,(\mathbf{V}^\star\,\gamma^\star - \mathbf{V}\,\gamma) && (53)\\ &= \boldsymbol{\Pi}^T\,\mathbf{V}\,\mathbf{U}\,(\mathbf{U}^{\star\,T}\,\gamma^\star - \mathbf{U}^T\,\gamma) && (54)\\ &= \mathbf{K}^{HR}\,\mathbf{U}\,(\mathbf{U}^{\star\,T}\,\gamma^\star - \mathbf{U}^T\,\gamma) && (55)\\ &\Rightarrow \gamma = \mathbf{U}\,\mathbf{U}^{\star\,T}\,\gamma^\star && (56)\\ &\Rightarrow \mathbf{q}_{HR} = \mathbf{q}^\star \text{ and } \boldsymbol{\sigma}^{HR} = \boldsymbol{\sigma}^\star && (57) \end{aligned}$$

Hence the hyper-reduced prediction is the same as the finite element prediction. But it uses less floating point operations.

In the sequel, we assume that there is a correlation between the approximation error $\boldsymbol{\sigma}^{HR} - \boldsymbol{\sigma}^\star$ in $\Omega_R^\star$, and the upper bound in Equation (40). This correlation is evaluated through a numerical experiment in Section 4.1.

3.3 Grassmannian ambient space

As explained in [28, 29], Grassmann manifolds are the adequate concept when considering interpolation of reduced order models. Property 3 shows that it is also relevant for data encoding in a proper ambient space and for the classification of voids according to their mechanical effects. We state that the target defect $\Omega^\star$ is similar to a defect having $\mathbf{V}$ for the ideal reduced basis, if the Chordal distance $d^{Ch}(\mathbf{V}^\star, \mathbf{V})$ is small enough. In the sequel, each defect in the training dataset is encoded by using its ideal reduced basis $\mathbf{V}^\star$, as shown in part (b) of Figure 1.

A common Grassmann manifold is defined for all defects by using a common encoding mesh. Each finite element prediction related to the training dataset of defects is transferred on this encoding mesh prior any machine learning, including singular value decomposition and dissimilarity computations. In order to facilitate the transfer of simulation data the prediction $\Delta\mathbf{u}^{\star(j)}$ is extended inside the defect, by introducing a very small Young modulus in the void ($10^{-3}\,E$). Figure 3 shows the chosen encoding mesh, with here 4 elements on each half-side of the middle square having a regular mesh.

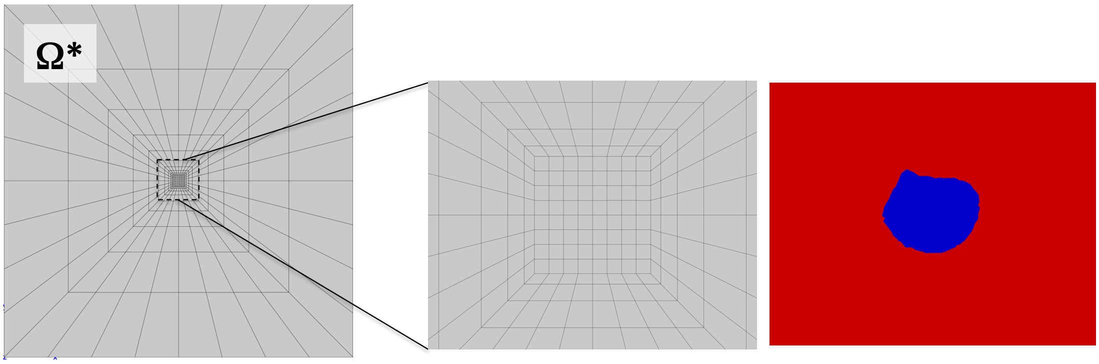

Figure 3: Encoding mesh with 4 elements on each half-side of the middle square having a regular mesh. From left to right, the surrounding box, a zoom, the same zoom on a defect.

This data encoding from the reduced mechanical response of the input, presents the huge advantage to be universal and may be applied in other fields. Each data in the dataset is supplemented by a reduced basis $\mathbf{V}^{\star(i)}$, here i is the defect index.

Several geodesic distances are available between points in Grassmann manifolds. The Chordal distance is one of them. The Grassmann distance is another one, more common in the literature. The Grassmann distance between the sub-spaces span by $\mathbf{V}^\star$ and $\mathbf{V}$ respectively is denoted by $d^{Gr}(\mathbf{V}^\star, \mathbf{V})$. It reads:

$$d^{Gr}(\mathbf{V}^\star, \mathbf{V}) = \frac{\|\boldsymbol{\theta}\|_2}{\pi/2} \tag{58}$$

In the following numerical experiment, the Grassmann distance magnifies the distance between sub-spaces compared to the Chordal distance, similarly to the one dimensional equation $\theta \geq \sin(\theta)$ for $\theta \in [0,\ \pi/2]$. As a result, we choose d^{Gr} for the partition of the training dataset of defects into classes of defects.

The encoding mesh must have a number of degrees of freedom $\mathcal{N}$ as small as possible to lower the memory usage in a storage system, but it must be fine enough:

- to lower the norm of transfer errors from the original mesh to the encoding mesh,
- to detect dissimilarities between defects, up to a given accuracy.

To highlight the influence of the encoding mesh on transfer errors, we varied the number of elements on each half-side of the middle square that have a regular mesh. Figure 4 presents the convergence of the Grassmann distance between a perfect circle and a isotropic defect or an anisotropic defect. Both isotropic and anisotropic defects are shown in Figure 5. Grassmann distances are calculated for several encoding meshes. The ideal reduced basis for the fluctuation modes around the circular defect is denoted by $\mathbf{V}^{\star(0)}$. $\mathbf{V}^{\star(1)}$ and $\mathbf{V}^{\star(2)}$ denotes the reduced bases related to the anisotropic defect and the isotropic one respectively. The two Grassmann distances are:

$$d_1 = d^{Gr}(\mathbf{V}^{\star(1)}, \mathbf{V}^{\star(0)}) \tag{59}$$

$$d_2 = d^{Gr}(\mathbf{V}^{\star(2)}, \mathbf{V}^{\star(0)}) \tag{60}$$

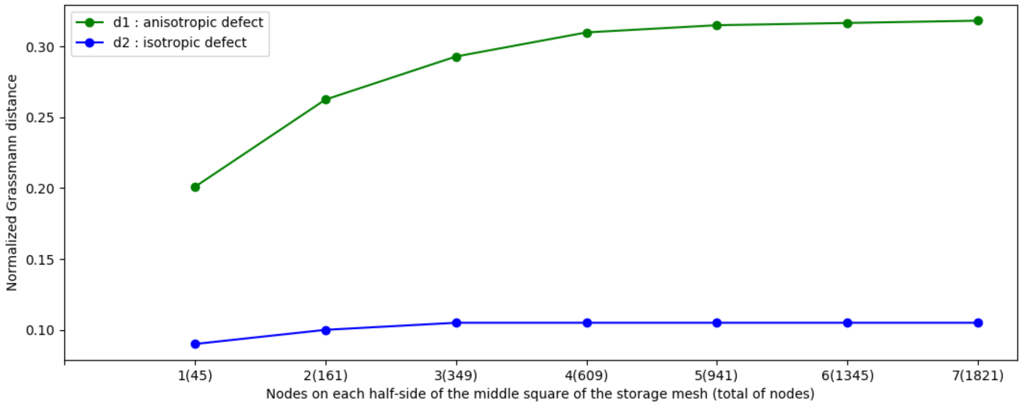

Figure 4: Convergence of the Grassmann distances with respect to the encoding mesh, for the evaluation of the dissimilarity between a circle and: an anisotropic defect (d_1) or a isotropic defect (d_2).

In Figure 4, the Grassmann distances and the encoding mesh successfully distinguish the two defects and we observe a convergence of the distances when the mesh exceeds 4 elements on each half-side of the middle square. A difference of 20% in the Grassmann distance between the two defects is consistent as the pilot circular defect and the anisotropic one are mechanically very different. The gap may be enough to distinguish them during the partition of training data. Therefore, we suggest to keep the encoding mesh with 609 nodes (4 elements on each half-side).

4 Numerical results on the training dataset of defects

3D images of voids have been obtained by Laurent Lacourt [20] via X-ray computed tomography of welded joints. These 3D images have been cut in slices so that we have more 2D samples. The dataset contains $n_I = 2,745$ samples of 2D images, with only one defect per image. But one defect may involve several voids that have a high mechanical interaction. 80% of these data have been randomly selected as training data. The remaining belongs to the test set.

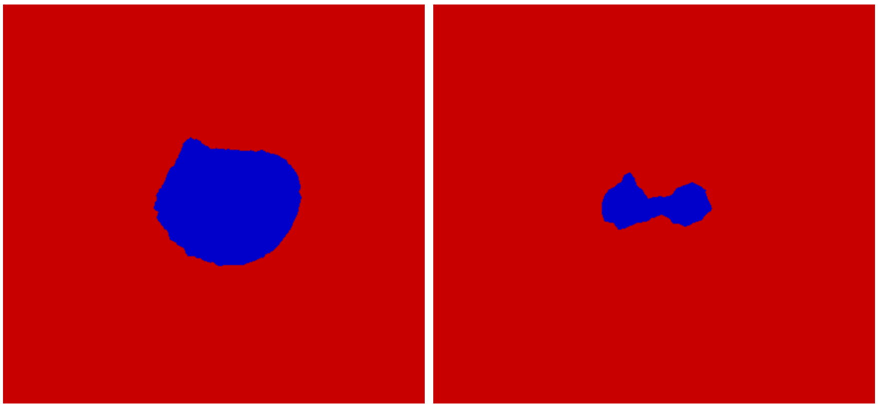

Figure 5: Examples of defects (defect in blue, steel in red). The isotropic defect is on the left, the anisotropic one, on the right.

4.1 Data clustering

Clustering methods have been already used for the construction of local reduced order bases in parametric spaces. We refer the reader to [38, 39] for instance and more recently in [40]. Local reduced order bases are known to be more accurate over a global reduced basis [38]. Here, the set of possible defects is not a parametric space. For this reason, k-means is useless because no barycentric coordinates are available here. The k-medoids algorithm [27] circumvent this difficulty in case of non parametric modeling via the selection of representative defects.

All available images in the dataset have been converted into finite element predictions via image-based digital twins. Displacement fluctuations have been transferred to the encoding mesh prior the computation of the related reduced basis $\mathbf{V}^{\star(i)}$ $(i = 1, \ldots, n_I)$. Then, a dissimilarity matrix has been computed, accounting for all the Grassmann distances between defects in the training dataset:

$$D^{Gr}_{ij} = d^{Gr}(\widehat{\mathbf{V}}^{\star(i)}, \widehat{\mathbf{V}}^{\star(j)}), \quad i, j \, \in \{1, \ldots, n_I\} \tag{61}$$

A k-medoids clustering [27] has been used for the partition of the data according to their Grassmann distance. The k-medoids algorithm proposed in [27] can be summarized as follows:

- Initialization step: select K rows in $\mathbf{D}^{Gr}$ as indices of initial medoids $(m_1, \ldots, m_K)$.
- Repeat the two following steps until convergence:
  - Data assignment step: assign each point of the dataset to the cluster corresponding to its closest medoid:

$$\mathcal{L}^{Gr}_i = \text{argmin}_{k \in \{1,\ldots,K\}} \left(\mathbf{D}^{Gr}[\, [m_1, \ldots, m_k, \ldots], \, i]\right) \quad i \in \text{training dataset} \tag{62}$$

  - Medoid update step: for each cluster, update the medoid by finding the point which minimizes the sum of distances to all the points in the cluster.

$$\begin{aligned} \mathcal{C}_k &= \{ i \in \text{training dataset} \,|\, \mathcal{L}^{Gr}_i = k \}, \quad k = 1, \ldots, K & (63) \\ m_k &= \text{argmin}_{j \in \mathcal{C}_k} \left(\sum_{i \in \mathcal{C}_k} \mathbf{D}^{Gr}[j, i] \right) & (64) \end{aligned}$$

We arbitrary set the number of clusters to $K = 5$. The set $\mathcal{C}_k$ contains the indices of defects in the cluster number k. Hence the size of the clusters are: $\text{card}(\mathcal{C}_1) = 554$, $\text{card}(\mathcal{C}_2) = 200$, $\text{card}(\mathcal{C}_3) = 202$, $\text{card}(\mathcal{C}_4) = 901$, $\text{card}(\mathcal{C}_5) = 339$.

The defects located in the medoids are shown in Figure 6. These defects have different anisotropies. m_4 is the most isotropic defect. m_2 and m_3 are the most anisotropic defects. These last defects are rather symmetric. In future work this symmetry should be removed from the dataset.

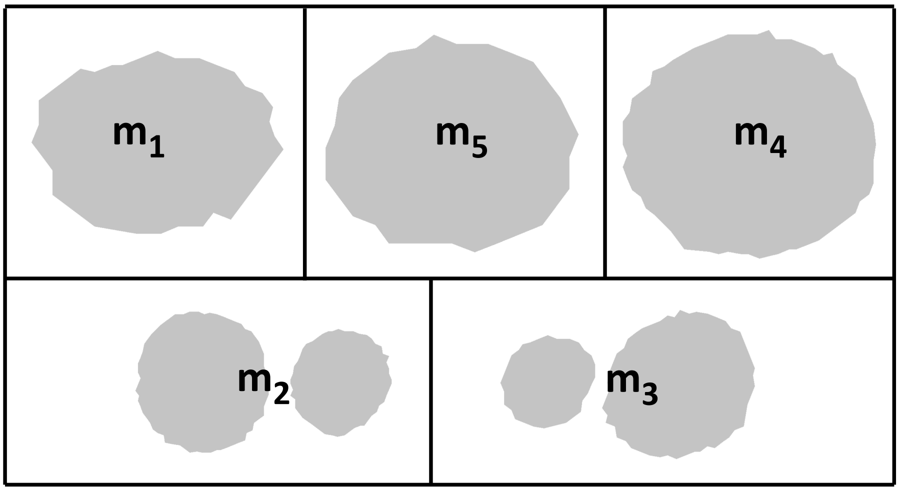

Figure 6: Defects located at the medoids.

Defects m_2 and m_3 contain two voids. They are so close to each other, that fluctuation modes account for the local interactions between these voids.

4.2 Validation of hyper-reduced predictions for the training dataset

The meta-parameters of hyper-reduction are setup by using the simulation data available in the training dataset.

For each medoid $m^{(k)}$ and for each target image number i, we define an image-specific hyper-reduced model denoted by $HR(k,i)$, without using the encoding mesh here. The hyper-reduced model corresponds to a couple of a reduced basis for displacement fluctuations and a reduced basis for stresses around defects, $(\mathbf{V}^{(k,i)}, \mathbf{V}^{\sigma\ (k,i)})$. These reduced bases are computed after the transfer of simulation data from the mesh of the medoid onto the mesh of the target problem which is defect-dependent. The matrix of macroscopic modes related to a defect-free mechanical problem is denoted $\mathbf{V}^{macro} \in \mathbb{R}^{\mathcal{N}^\star \times 3}$. The column number j in $\mathbf{V}^{macro}$ is related to the macroscopic displacement $\mathbf{E}^{(j)}\ \mathbf{x}$. The complete reduced basis for displacement reads:

$$\overline{\mathbf{V}}^{(k,i)} = [\mathbf{V}^{macro},\ \mathbf{V}^{(k,i)}] \in \mathbb{R}^{\mathcal{N}^\star \times 6}$$

The hyper-reduced equilibrium equation is Equation (13) with empirical modes obtained by substituting $\mathbf{V}^{(k,i)}$ for $\mathbf{V}$ in Equation (8). A zone of interest is designed automatically around each defect. It contains 4 layers of elements from the border of the defect $\partial_V \Omega^\star$. The construction of the RID follows the procedure explained in Appendix, so that $\Omega_R^\star$ contains the zone of interest.

For each image #i in the training dataset, a hyper-reduced model is built. It is denoted by $HR(k,i)$, for each medoid ($k = 1, \ldots, 5$). HR predictions are performed for the three macroscopic strains $\mathbf{E}^{(j)}$ ($j = 1, \ldots, 3$). The predicted stresses on the RID are denoted by $\sigma^{HR\ (k,i,j)}$. The finite element prediction of this stress is denoted by $\sigma^{\star\ (i,j)}$. The exact error on the stress prediction in ${\Omega_R^\star}^{(i)}$, $i \in \{1, \ldots, n_I\}$, reads:

$$e^{HR(k,i)} = 100 \sqrt{\frac{\sum_{j=1}^{3} \|\sigma^{\star\ (i,j)} - \sigma^{HR\ (k,i,j)}\|^2_{\Omega_R}}{\sum_{j=1}^{3} \|\sigma^{\star\ (i,j)}\|^2_{\Omega_R}}} \tag{65}$$

where $\| \cdot \|_{\Omega_R} = \int_{\Omega_R} \cdot : \cdot \, d\Omega$ for stress tensors. Figure 7 reports the correlation between the exact error $e^{HR(k,i)}$ and the Chordal distance to the medoid. This plot contains $5 \times n_I$ points. The coordinates of these points are $(D^{Ch}_{m_k,i},\ e^{HR(k,i)})$. The average Chordal distance is 0.7. The average error is 29%.

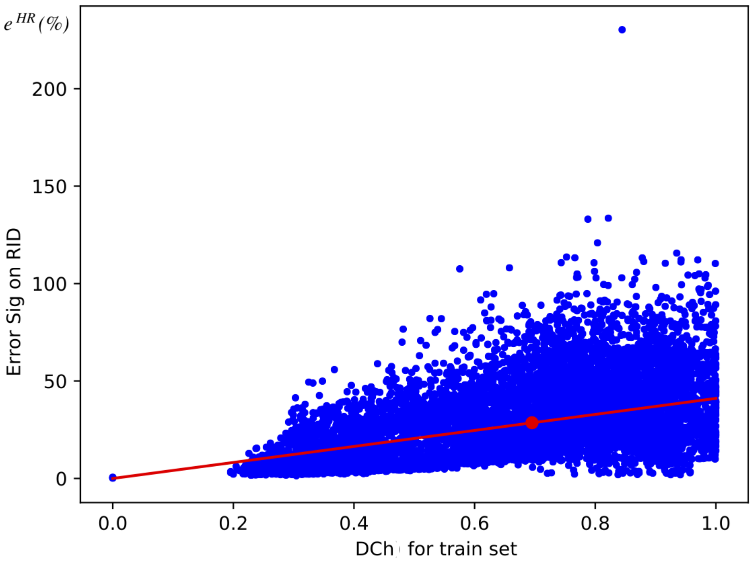

Figure 7: Correlation plot between $e^{HR(k,i)}$ and d^{Ch} for all points in the training dataset and for all hyper-reduced models. The red dot is the average point ($x = 0.7$, $y = 29\%$)

The correlation between e^{HR} and d^{Ch} is not perfect, but it is sufficient here for the clustering of simulation data. In some situations, e^{HR} and d^{Ch} may not be correlated. A good correlation requires that the target mechanical problem activates all the modes in $\mathbf{V}^{\star(i)}$ and $\mathbf{V}^{(k,i)}$, meaning that the related reduced coordinates have no null component. It is the case here. If one of the reduced component is null, the upper bound can be obviously simplified without using all the principal angles in $d^{Ch}(\mathbf{V}^{\star(i)}, \mathbf{V}^{(k,i)})$.

For each cluster of data we have reported in figures 8 to 12 the histograms of the density distribution of $e^{HR(k,i)}$, for $i \in \mathcal{C}_k$, inside each cluster separately.

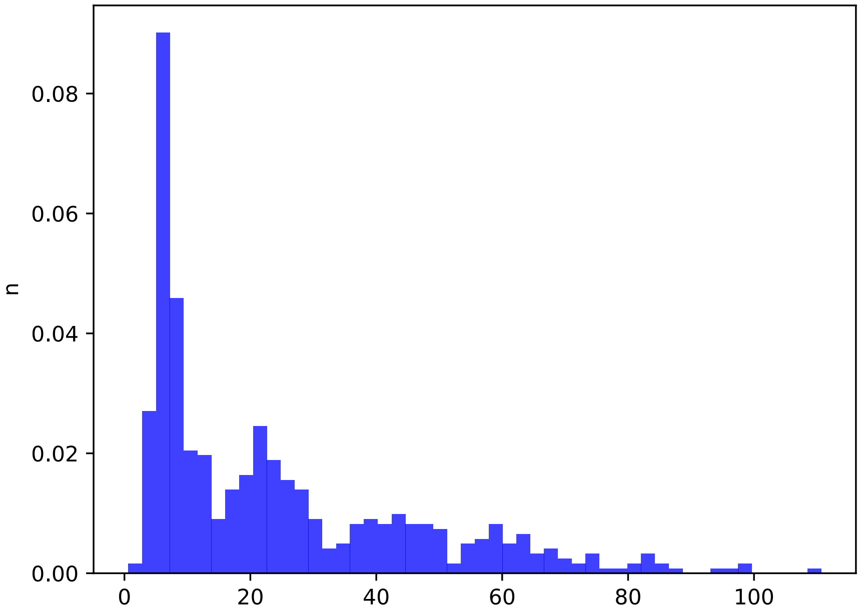

Figure 8: Density distribution for $e^{HR(1,i)}$ (%) in cluster #1, for $i \in \mathcal{C}_1$.

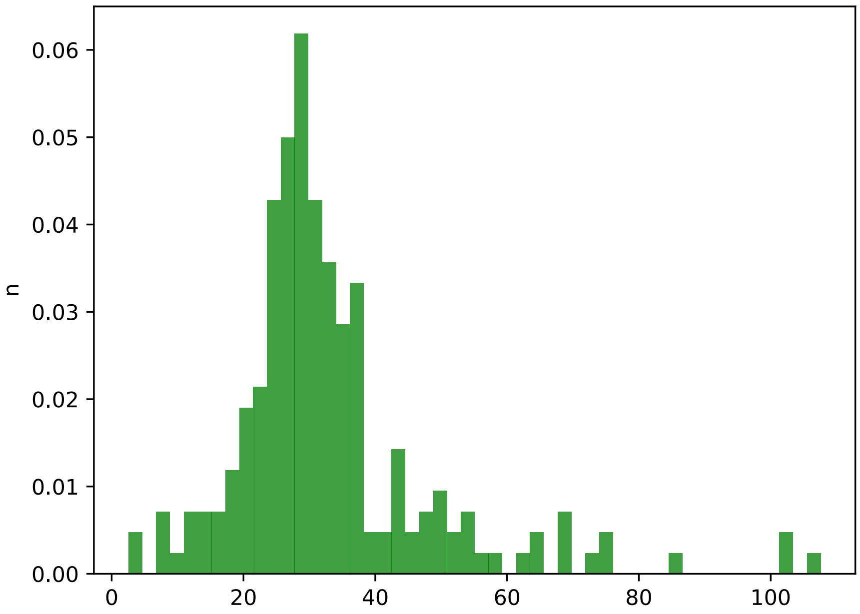

Figure 9: Density distribution for $e^{HR(2,i)}$ (%) in cluster #2, for $i \in \mathcal{C}_2$.

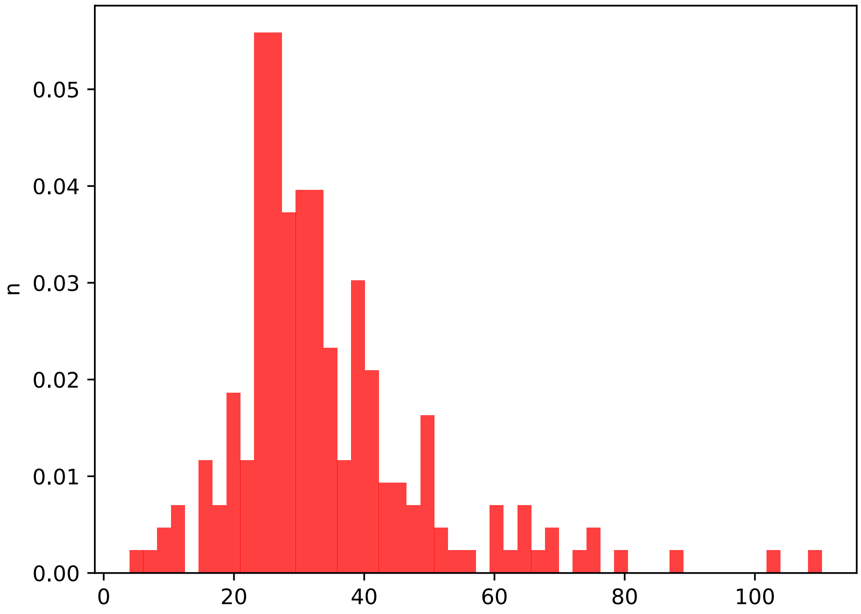

Figure 10: Density distribution for $e^{HR(3,i)}$ (%) in cluster #3, for $i \in \mathcal{C}_3$.

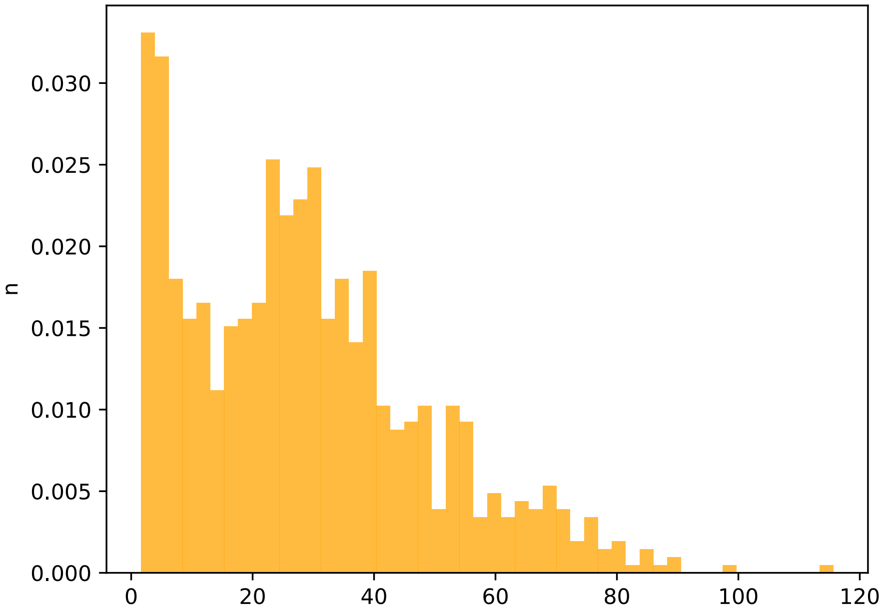

Figure 11: Density distribution for $e^{HR(4,i)}$ (%) in cluster #4, for $i \in \mathcal{C}_4$.

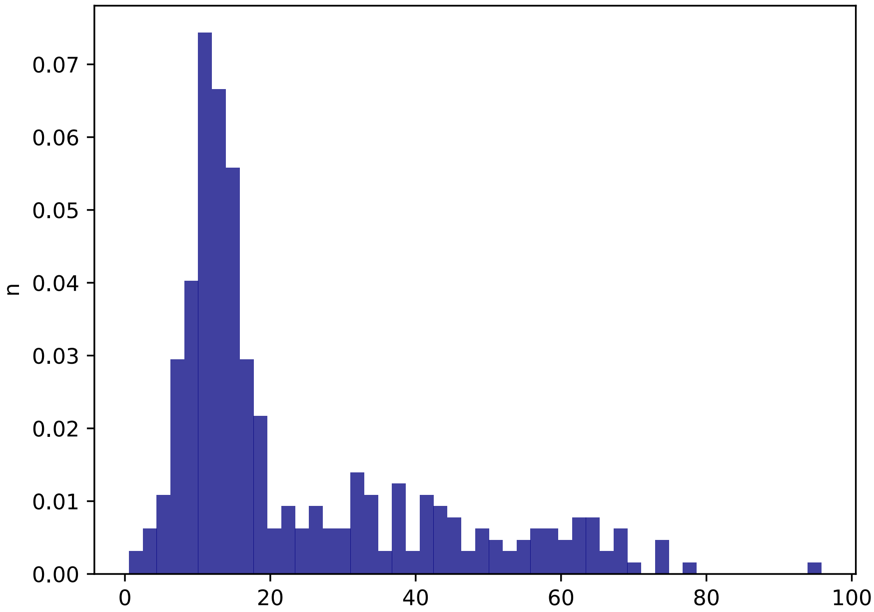

Figure 12: Density distribution for $e^{HR(5,i)}$ (%) in cluster #5, for $i \in \mathcal{C}_5$.

The clustering results are interesting because, most of errors are below 29% (the average error on all the dataset). But many points have an error e^{HR} bigger than 20%. The clustering may not perform well for clusters where there is a lack of similar data. Here clusters $\mathcal{C}_2$ and $\mathcal{C}_3$ have few points with an error lower than 20%.

Some clusters could be rejected for hyper-reduction, in a sense that a full finite element prediction may be preferable for the defects in these clusters. In the sequel we don't reject any cluster, and we include simulation data related to all the medoids in the dictionary of digital twins.

5 Results on the test set of defects

5.1 Selection of a reduced digital twin in the dictionary

In this section, we restrict our attention to simulation data in the test set. This test set aims to evaluate the full modeling procedure for fast prediction of stresses around defects. The average speed up for the solution of linear systems is $\frac{0.03}{0.003} = 10$ for hyper-reduced predictions. The average speed up for the computation of the stresses, in this equation, is $\frac{0.01}{0.005} = 2$. Speedups around 1000 are obtained for similar 3D problems [20].

An error indicator has been developed for the selection in the dictionary of the medoid that is expected to give the best stress prediction via hyper-reduction. This error indicator is similar to the error $e^{HR(k,i)}$ where the exact stress $\boldsymbol{\sigma}^\star$ is replaced by the equilibrated stress $\boldsymbol{\sigma}^{eq}$. The error indicator reads:

$$\eta^{(k,i)} = 100 \sqrt{\frac{\sum_{j=1}^{3} \|\delta\sigma^{(k,i,j)}\|^2_{\Omega_R}}{\sum_{j=1}^{3} \|\sigma^{eq\,(i,j)}\|^2_{\Omega_R}}} \tag{66}$$

where $\delta\sigma^{(k,i,j)}$ is the stress correction, in Equation (23), computed by the equilibrium step related to HR (k,i).

For each defect in the test set, we select a medoid $k^{\star(i)}$ for stress prediction such that:

$$k^{\star(i)} = \text{argmin}_k \eta^{(k,i)} \tag{67}$$

The best medoid selection aims to lower the error prediction on stresses:

$$\overline{k}^{\star(i)} = \text{argmin}_k e^{HR(k,i)} \tag{68}$$

Then we get an automatic labeling of the defects in the test set. The estimated labels are denoted by $\mathcal{L}_i^\eta$: $\mathcal{L}_i^\eta = \text{argmin}_k \eta^{(k,i)}$. The perfect labels are denoted by $\mathcal{L}_i$: $\mathcal{L}_i = \text{argmin}_k e^{HR(k,i)}$. Figure 13, reports the correlation between $e^{HR(k,i)}$ and the error indicator $\eta^{(k,i)}$.

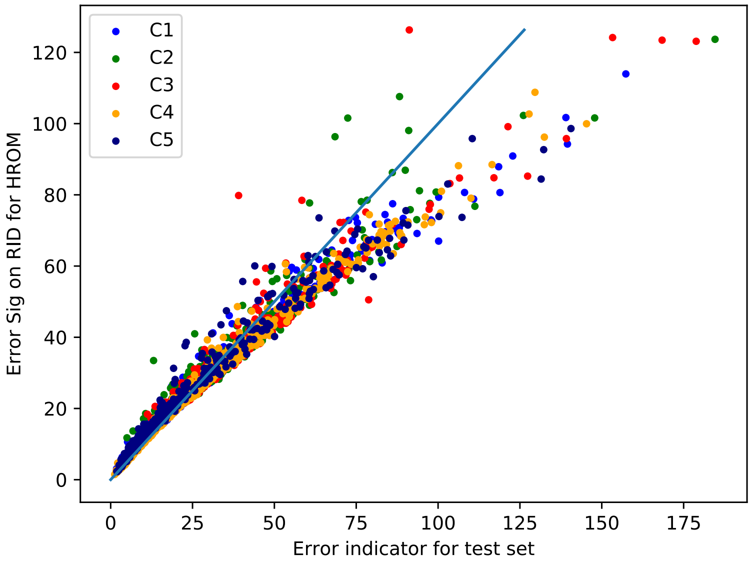

Figure 13: Correlation plot between $e^{HR(k,i)}$ and $\eta^{(k,i)}$ for points in the test set. The dot color is related to the cluster index k.

There is a strong correlation between $e^{HR(k,i)}$ and $\eta^{(k,i)}$ for low errors: $e^{HR(k,i)} \approx \eta^{(k,i)}$ for $e^{HR(k,i)} < 40\%$. This correlation exists for every cluster. As a result, this indicator helps to find the medoid as if we have the exact finite element prediction.

The better $\boldsymbol{\sigma}^{eq}$ approximates $\boldsymbol{\sigma}^{\star}$, the more accurate the error indicator. The error on equilibrated stresses reads:

$$e^{eq(k,i)} = 100 \sqrt{\frac{\sum_{j=1}^{3} \|\sigma^{\star\,(i,j)} - \sigma^{eq\,(k,i,j)}\|^2_{\Omega_R}}{\sum_{j=1}^{3} \|\sigma^{\star\,(i,j)}\|^2_{\Omega_R}}} \tag{69}$$

The Figure 14 shows the correlation between $e^{eq(k,i)}$ and $\eta^{(k,i)}$. Such a correlation is sufficient to select the same hyper-reduced order model for the predictions with or without an equilibrium step. The range of errors on equilibrated stresses is much smaller than the one on $\boldsymbol{\sigma}^{HR}$. Therefore, the equilibrated stresses are the simulation outputs of interest for the reduced digital twin.

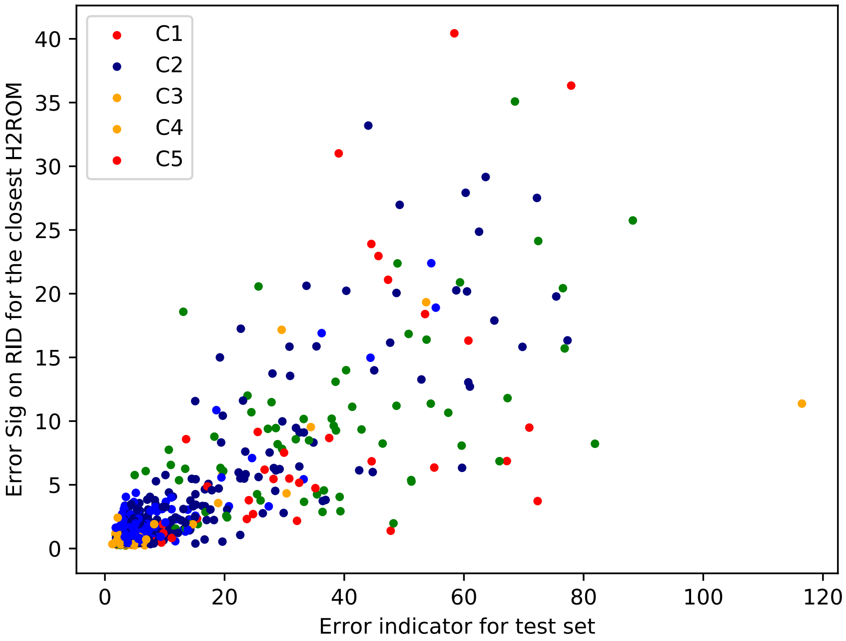

Figure 14: Correlation plot between $e^{eq(k,i)}$ and $\eta^{(k,i)}$ for points in the test set. The spot color is related to the cluster index k.

For each cluster of data we have reported on figures 15 to 19 the histograms of the density distribution of $e^{eq(k,i)}$, for $\mathcal{L}_i^{\eta} = k$, inside each cluster separately.

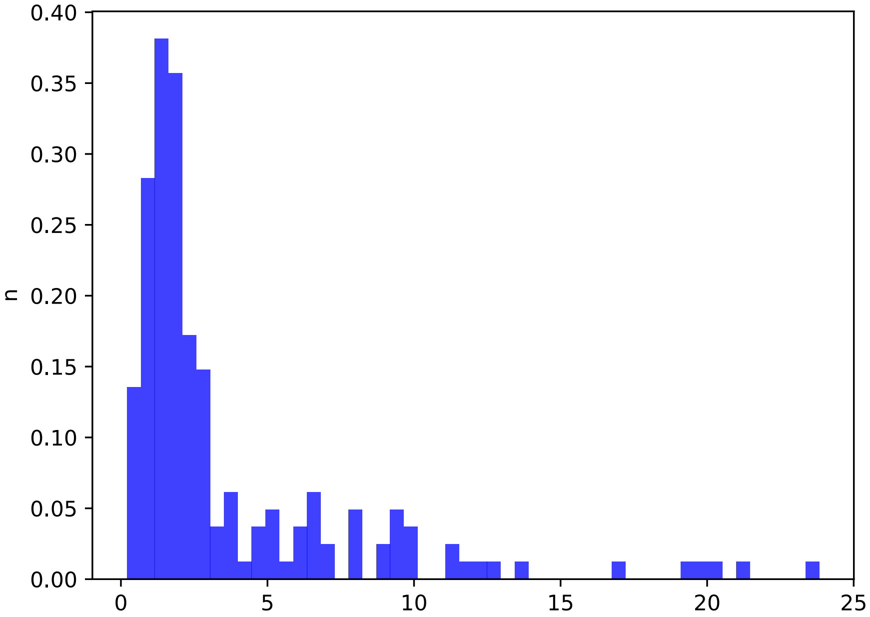

Figure 15: Density distribution for $e^{eq(1,i)}$ (%) in cluster #1, for $\mathcal{L}_i^{\eta} = 1$.

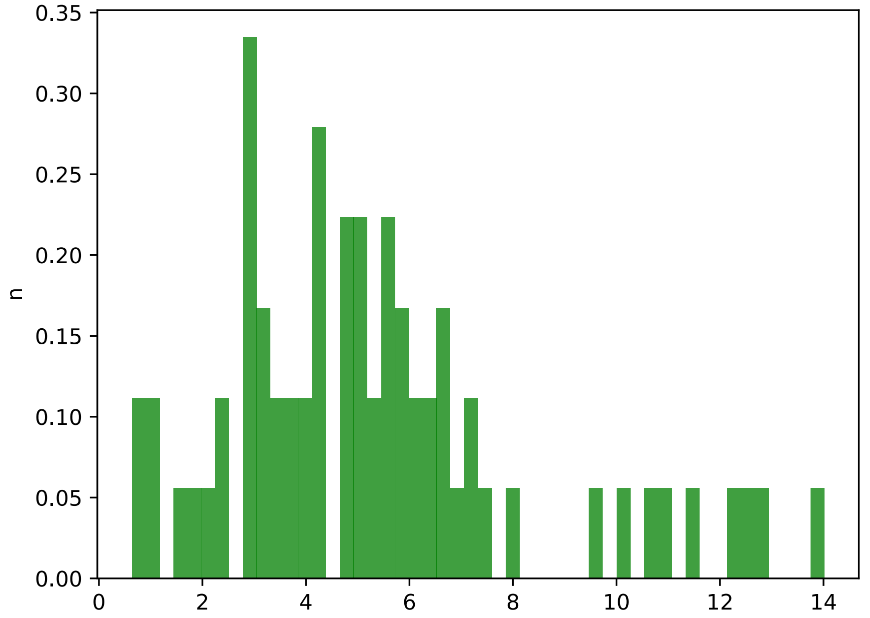

Figure 16: Density distribution for $e^{eq(2,i)}$ (%) in cluster #2, for $\mathcal{L}_i^{\eta} = 2$.

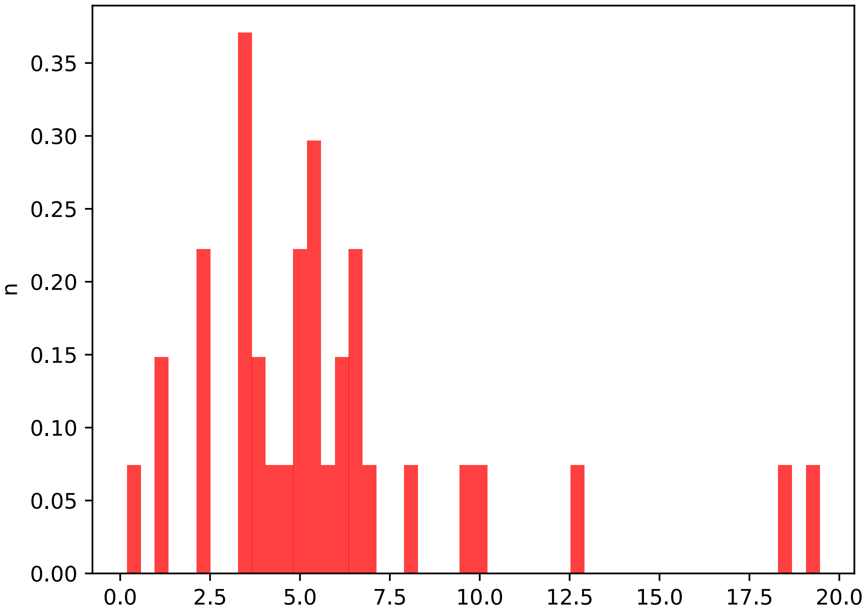

Figure 17: Density distribution for $e^{eq(3,i)}$ (%) in cluster #3, for $\mathcal{L}_i^\eta = 3$.

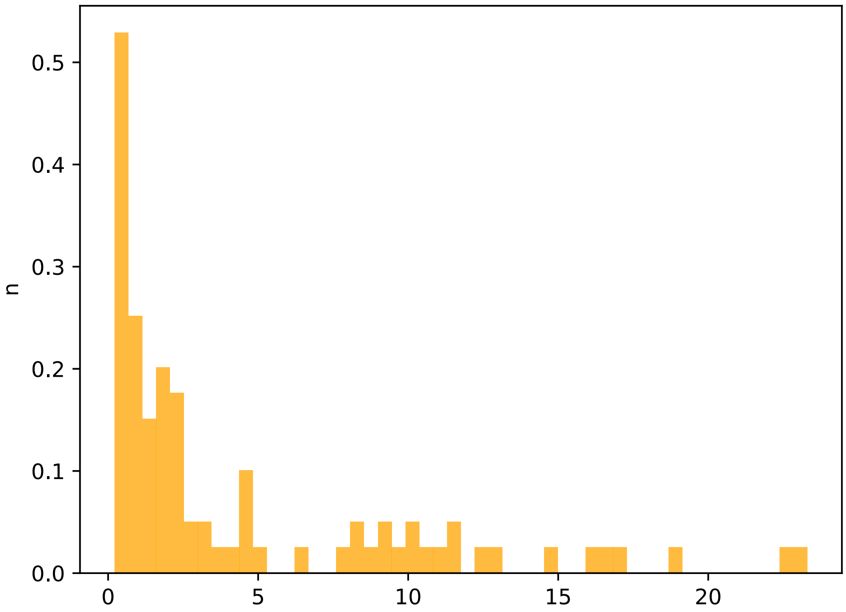

Figure 18: Density distribution for $e^{eq(4,i)}$ (%) in cluster #4, for $\mathcal{L}_i^\eta = 4$.

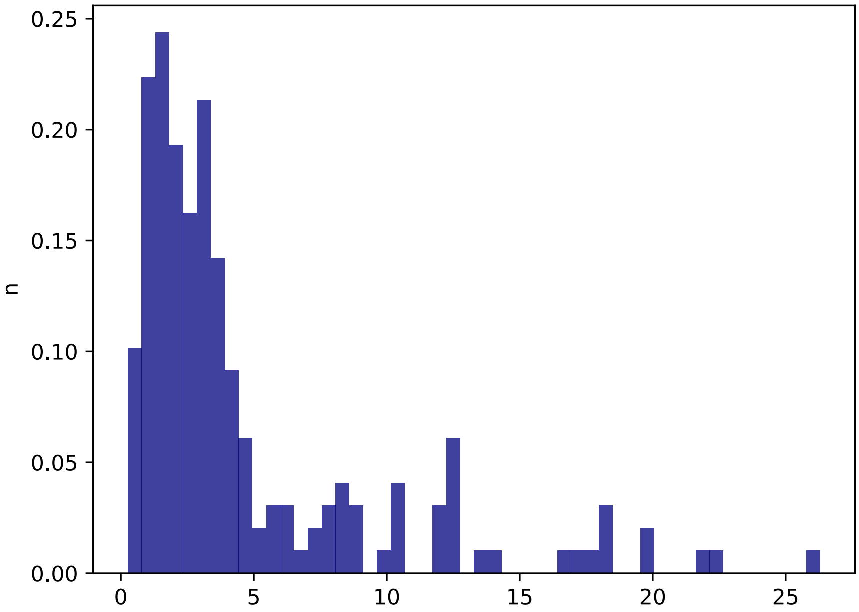

Figure 19: Density distribution for $e^{eq(5,i)}$ (%) in cluster #5, for $\mathcal{L}_i^\eta = 5$.

Most of errors on equilibrated stresses are lower than 5%. The modeling procedure is very accurate. Errors related to medoids m_1, m_4 and m_5 are more concentrated below 5% than for medoids m_2 and m_3. Hyper-reduced predictions attached to medoids m_2 and m_3 are less accurate. Such results have been anticipated during the clustering procedure.

5.2 Detailed numerical results on hyper-reduced predictions

In this section we report local numerical results for defects in the test set. The index of the first image is $i = 1664$. Its label via the error indicator is $\mathcal{L}_i^\eta = 3$. This label is the optimal: $\mathcal{L}_i^\eta = \mathcal{L}_i$. It is intentionally related to a medoid of the small cluster $\mathcal{C}_3$, for which there is certainly a lack of observed defects. The prediction is globally accurate $e^{eq(3,\,1664)} = 5\%$.

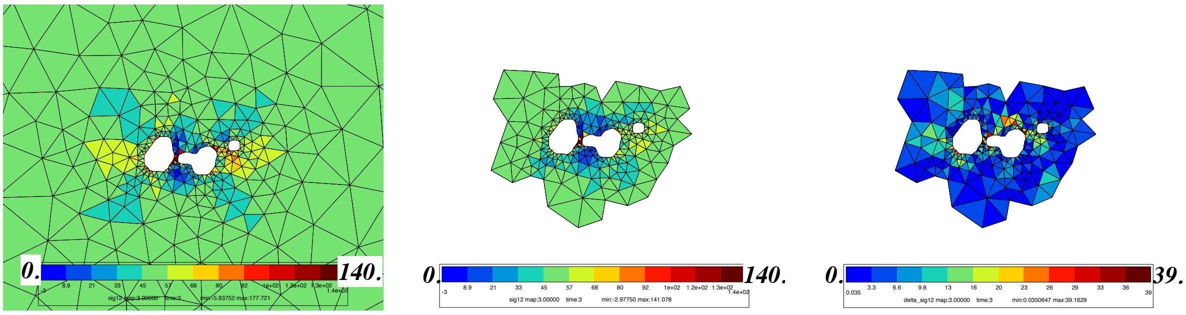

Figure 20: Test defect #1664, from left to right: finite element prediction of the shear stress related to $\mathbf{E}^{(3)}$, the related equilibrated stress σ^{eq} on the RID around the defect, the error map for this stress component.

Better results are obtained for test data attached to m_4, the medoid of the largest cluster. The index of the second image is $i = 1987$. The global error is $e^{eq(4,\,1987)} = 0.2\%$. Local predictions of the shear stress for $\mathbf{E}^{(3)}$ are reported in Figure 21.

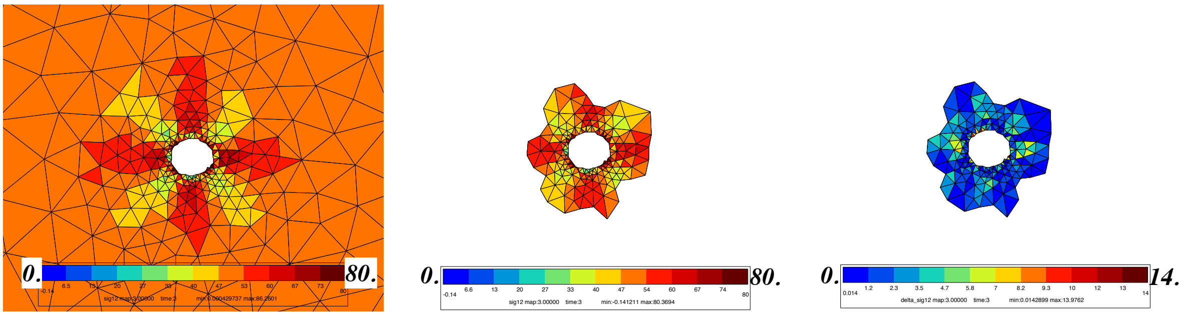

Figure 21: Test defect #1987, from left to right: finite element prediction of the shear stress related to $\mathbf{E}^{(3)}$, the related equilibrated stress σ^{eq} on the RID around the defect, the error map for this stress component.

Local predictions are very accurate for this defect, certainly because cluster $\mathcal{C}_4$ involves a large number of observed defects.

6 Conclusion

Hyper-reduction of linear elastic problems with non-parametric variations is an opportunity to propose new theoretical results on the convergence of partial errors on stress predictions. The upper bound of this partial error scales with a distance between an ideal reduced basis of fluctuation modes and the reduced basis involved in the hyper-reduced prediction. These two reduced bases span vector sub-spaces that belong to the same Grassmann manifold. Hence, the metrics related to a Grassmann manifold enables to define the dissimilarity of defects. It accounts for the mechanical effects of the defect in terms of displacement fluctuation modes. Defects that have similar fluctuation modes are considered as similar defects because they have similar hyper-reduced order models. Hence data in the training dataset are considered as points in a Grassmannian ambient space.

A k-medoids algorithm selects representative defects in the training dataset. These representative defects are saved in the dictionary of digital twins. They are optimally distributed according to Grassmann distances between all defects in the training dataset. The simulation data of the representative defects are the training data used for the hyper-reduction of digital twins.

For defects in the test set, or for new observed defects, a classifier sets a label that selects the best item in the dictionary of digital twins. This is an automatic labeling performed via an error indicator related to the discrepancy between the stresses predicted by hyper-reduction and an equilibrated stress field. Both stress predictions are restricted to a reduced integration domain. Equilibrated stresses are much more accurate than hyper-reduced stress predictions. Errors lower than 5% on equilibrated stress predictions are achieved by the proposed dictionary of digital twins.

The higher the speedup obtained by hyper-reduced predictions, the larger the number of medoids saved in the dictionary of digital twins. A study on 3D images would be more relevant for a speedup analysis. Indeed, the computational complexity of medoid selection for test data is proportional to the hyper-reduction speedup times the number of items in the dictionary. For large number of medoids, ROM-nets are available to accelerate this selection by using deep classifiers. But such machine-learning approaches require data augmentation schemes.

Many strong hypotheses have been made here. Only elastic deformation has been considered, with low stresses applied in consequence. However, plasticity is widely present when fractures and harmfulness of defects are studied. The mechanical response of the defect, and therefore the classification, would change if plasticity was studied. But elastic classification of defects can be understood as a first classification step, because plastic transformations usually start with elastic strains.

Appendix: details about the RID construction

Let's introduce two mathematical operators. The first one, collects the degrees of freedom of a sub-domain Ω_α:

$$\mathcal{C}(\Omega_\alpha) = \{i \in \{1, \dots \mathcal{N}\}, \int_{\Omega_\alpha} \boldsymbol{\varphi}_i^2 \, d\Omega > 0\}$$

The second one aggregates the support of FE shape functions having their index in a set $\mathcal{G}$:

$$\mathcal{L}(\mathcal{G}) = \cup_{i \in \mathcal{G}} \text{supp}(\boldsymbol{\varphi}_i), \quad \mathcal{L}(\mathcal{G}) \subset \Omega$$

The extension of this subdomain by adding n layers of connected elements reads:

$$(\mathcal{L} \circ \mathcal{C})^n \circ \mathcal{L}(\mathcal{G})$$

The operator $\mathcal{L}$ is fine for displacement fields, because they are approximated by the FE shape functions. A similar operator is also introduced for stresses. When collecting simulation data related to stresses, in the matrix $\mathbf{Q}^\sigma$, we store all the stress components at all Gauss points for all elements. Each row of $\mathbf{Q}^\sigma$ is related to one component of the stress tensor, at a Gauss point in an element. Then, the DEIM algorithm applied to $\mathbf{V}^\sigma$ gives a set of indices of components of the stress tensor, at some Gauss points in some elements. This set is denoted by $\mathcal{P}^\sigma$. We denote by $\mathcal{L}^\sigma(\mathcal{P}^\sigma)$ the support of the elements related to set $\mathcal{P}^\sigma$. $\mathcal{L}^\sigma(\mathcal{P}^\sigma)$ is a subdomain of Ω.

In this paper, the RID construction was the following:

$$\Omega_R = (\mathcal{L} \circ \mathcal{C}) \circ (\mathcal{L}(\mathcal{P}) \cup \mathcal{L}^\sigma(\mathcal{P}^\sigma)) \cup \Omega_{ZOI}$$

where Ω_{ZOI} is the zone of interest.

References

[1] Z. Li, X. Yan, C. Yuan, Z. Peng, and L. Li. Virtual prototype and experimental research on gear multi-fault diagnosis using wavelet-autoregressive model and principal component analysis method. *Mechanical Systems and Signal Processing*, 25:2589–2607, 2011.

[2] T Mira-Aguiar, C Leitão, and DM Rodrigues. Solid-state resistance seam welding of galvanized steel. *The International Journal of Advanced Manufacturing Technology*, 86(5):1385–1391, Sep 2016.

[3] T Uwaba, Y Yano, and M Ito. Resistance spot weldability of 11cr-ferritic/martensitic steel sheets. *Journal of Nuclear Materials*, 421(1):132 – 139, 2012.

[4] SK Dinda, JM Warnett, MA Williams, GG Roy, and P Srirangam. 3d imaging and quantification of porosity in electron beam welded dissimilar steel to fe-al alloy joints by x-ray tomography. *Materials and Design*, 96:224 – 231, 2016.

[5] JD Madison and L K Aagesen. Quantitative characterization of porosity in laser welds of stainless steel. *Scripta Materialia*, 67(9):783 – 786, 2012.

[6] A Haboudou, P Peyre, AB Vannes, and G Peix. Reduction of porosity content generated during nd:yag laser welding of a356 and aa5083 aluminium alloys. *Materials Science and Engineering: A*, 363(1):40 – 52, 2003.

[7] David Amsallem and Charbel Farhat. An online method for interpolating linear parametric reduced-order models. *SIAM J Sci Comput.*, 33:2169–2198, 2011.

[8] S. Moomkesh, S.A. Mireei, M. Sadeghi, and M. Nazeri. Early detection of freezing damage in sweet lemons using vis/swnir spectroscopy. *Biosystems Engineering*, 164:157–170, 2017.

[9] Y. Le Cun, B. Boser, J.S. Denker, D. Henderson, R.E. Howard, W. Hubbard, and et al. L.D. Jackel. Hand-written digit recognition with a back-propagation network. *Advances in neural information processing systems*, 1990.

[10] A. Krizhevsky, I. Sutskever, and G.E. Hinton. Imagenet classification with deep convolutional neural networks. *Advances in Neural Information Processing Systems*, 2:1097–1105, 2012. cited By 33336.

[11] T. Zehelein, T. Hemmert-Pottmann, and M. Lienkamp. Diagnosing automotive damper defects using convolutional neural networks and electronic stability control sensor signals. *Sensor and Actuator Networks*, pages 1–19, 2020.

[12] Ling Xiao, Bo Wu, Youmin Hu, and Jiwei Liu. A hierarchical features-based model for freight train defect inspection. *IEEE Sensors Journal*, 20:2671–2678, 2020.

[13] S. J. Pan and Q. Yang. A survey on transfer learning. *IEEE Transactions on Knowledge and Data Engineering*, 22(10):1345–1359, 2010.

[14] D. Ulrich, B. [van Rietbergen], H. Weinans, and P. Ruegsegger. Finite element analysis of trabecular bone structure: a comparison of image-based meshing techniques. *Journal of Biomechanics*, 31(12):1187 – 1192, 1998.

[15] F N'Guyen. *Morphologie mathématique appliquée au développement d'outils de maillage EF automatiques dans le cas de microstructures hétérogènes bi et multiphasées*. PhD thesis, Lille 1 University, 2014.

[16] Proudhon Henry, Guéninchault Nicolas, Forest Samuel, and Ludwig Wolfgang. Incipient bulk polycrystal plasticity observed by synchrotron in-situ topotomography. *Materials*, 11, 2018.

[17] Yasin Amani, Sylvain Dancette, Pauline Delroisse, Aude Simar, and Eric Maire. Compression behavior of lattice structures produced by selective laser melting: X-ray tomography based experimental and finite element approaches. *Acta Materialia*, 159:395 – 407, 2018.

[18] Anna Madra, Piotr Breitkopf, Alain Rassineux, and François Trochu. Image-based model reconstruction and meshing of woven reinforcements in composites. *International Journal for Numerical Methods in Engineering*, 112(9):1235–1252, 2017.

[19] Yujie Huang, Zhenjun Yang, Wenyuan Ren, Guohua Liu, and Chuanzeng Zhang. 3d meso-scale fracture modelling and validation of concrete based on in-situ x-ray computed tomography images using damage plasticity model. *International Journal of Solids and Structures*, 67-68:340 – 352, 2015.

[20] Laurent Lacourt, David Ryckelynck, Samuel Forest, Victor de Rancourt, and Sylvain Flouriot. Hyper-reduced direct numerical simulation of voids in welded joints via image-based modeling. *International Journal for Numerical Methods in Engineering*, n/a(n/a), 2020.

[21] D. Ryckelynck. Hyper-reduction of mechanical models involving internal variables. *International Journal for Numerical Methods in Engineering*, 77(1):75–89, 2009.

[22] Thomas Daniel, Fabien Casenave, Nissrine Akkari, and David Ryckelynck. Model order reduction assisted by deep neural networks (rom-net). *Advanced Modeling and Simulation in Engineering Sciences*, 7(1):16, 2020.

[23] J Lumley. The structure of inhomogeneous turbulence. *Atmospheric turbulence and wave propagation*, Nauka,Moscow:166–178, 1967.

[24] M. Raissi, P. Perdikaris, and G.E. Karniadakis. Physics-informed neural networks: A deep learning framework for solving forward and inverse problems involving nonlinear partial differential equations. *Journal of Computational Physics*, 378:686 – 707, 2019.

[25] Franck Nguyen, Selim M. Barhli, Daniel Pino Muñoz, and David Ryckelynck. Computer vision with error estimation for reduced order modeling of macroscopic mechanical tests. *Complexity*, 2018.

[26] Laurent Lacourt. *Lifetime assessment of welded structures containing defects.* PhD thesis, Mines ParisTech-PSL University, 2019.

[27] Park HS and Jun CH. A simple and fast algorithm for k-medoids clustering. *Expert Systems with Applications*, 36:3336–3341, 2009.

[28] D. Amsallem and C. Farhat. Interpolation method for adapting reduced-order models and application to aeroelasticity. *AIAA Journal*, 46:1803–1813, 2008.

[29] R. Mosquera, A. Hamdouni, A. El Hamidi, and C. Allery. Pod basis interpolation via inverse distance weighting on grassmann manifolds. *Discrete and Continuous Dynamical Systems, Series S*, 12:1743–1759, 2018.

[30] K. Ye and L.H. Lim. Schubert varieties and distances between subspaces of different dimensions. *SIAM J. Matrix Anal. Appl.*, 37(3):1176–1197, 2016.

[31] D Ryckelynck, K Lampoh, and S Quilici. Hyper-reduced predictions for lifetime assessment of elasto-plastic structures. *Meccanica*, 51:309–317, 2016.

[32] M. Barrault, Y. Maday, N. C. Nguyen, and A. T. Patera. An empirical interpolation method: application to efficient reduced-basis discretization of partial differential equations. *Comptes Rendus Mathématiques*, 339(9):667 – 672, 2004.

[33] J Fauque, I Ramiere, and D Ryckelynck. Hybrid hyper-reduced modeling for contact mechanics problems. *International Journal for Numerical Methods in Engineering*, 115(1):117–139, JUL 6 2018.

[34] J. Baiges, R. Codina, and S. Idelson. A domain decomposition strategy for reduced order models. application to the incompressible navier-stokes equations. *Computer Methods in Applied Mechanics and Engineering*, 267:23–42, 2013.

[35] P. Kerfriden, J. C. Passieux, and S. Bordas. Local/global model order reduction strategy for the simulation of quasi-brittle fracture. *International Journal for Numerical Methods in Engineering*, 89(2):154–179, 2012.

[36] P. Kerfriden, J. J. Ródenas, and S. P.-A. Bordas. Certification of projection-based reduced order modelling in computational homogenisation by the constitutive relation error. *International Journal for Numerical Methods in Engineering*, 97(6):395–422, 2014.

[37] K.C. Hoang, P. Kerfriden, and S.P.A. Bordas. A fast, certified and "tuning free" two-field reduced basis method for the metamodelling of affinely-parametrised elasticity problems. *Computer Methods in Applied Mechanics and Engineering*, 298:121 – 158, 2016.

[38] Samir Sahyoun and Seddik M. Djouadi. Control of nonlinear pdes based on space vectors clustering reduced order systems. *IFAC Proceedings Volumes*, 47(3):5181 – 5186, 2014. 19th IFAC World Congress.

[39] Mohamadreza Ghasemi and Eduardo Gildin. Localized model reduction in porous media flow. *IFAC-PapersOnLine*, 48(6):242 – 247, 2015. 2nd IFAC Workshop on Automatic Control in Offshore Oil and Gas Production OOGP 2015.

[40] Martin Hess, Alessandro Alla, Annalisa Quaini, Gianluigi Rozza, and Max Gunzburger. A localized reduced-order modeling approach for pdes with bifurcating solutions. *Computer Methods in Applied Mechanics and Engineering*, 351:379 – 403, 2019.